CERN-THESIS-2009-213

Diplomarbeit

Kinematic Fits to Determine Masses of Supersymmetric Particles at LHC

Hannes Schettler

April 2009

Gutachter:
Prof. Dr. Peter Schleper
Prof. Dr. Johannes Haller

Institut für Experimentalphysik
Universität Hamburg

Abstract

In this thesis the method of kinematic fits is applied to determine the masses of supersymmetric particles. This is implemented by a constrained least square fit. If Supersymmetry is realized with R-parity conservation, the produced supersymmetric particles decay directly or over a cascade into the lightest supersymmetric particle (LSP) which has to be stable and escapes undetected. Each massive particle in the decay chain can be used as a constraint on the invariant mass. With such constraints the unmeasurable momentum components of the LSPs can be reconstructed.

The masses of the Susy particles enter the fit as hypotheses. By scanning over the masses the fit is redone with different hypotheses. The χ^2 of the fit is suitable to distinguish between good and bad hypotheses. Therefore the method can be used to measure the mass parameters. The technique is presented by means of the Susy model mSUGRA. The branches of the signal cascade are $\tilde{g} \to \tilde{q} \to \chi_2^0/\chi_1^\pm \to \chi_1^0(\text{LSP})$ and $\tilde{q} \to \chi_2^0/\chi_1^\pm \to \chi_1^0(\text{LSP})$.

The challenges are the selection of the jets belonging to the cascade, the combinatorial background, and the background from other Susy events. This study shows that kinematic fits are capable to exclude regions in the parameter space and to indicate where the true masses lie.

Zusammenfassung

In dieser Arbeit wird die Methode der kinematischen Fits zur Massenbestimmung supersymmetrischer Teilchen angewendet. Dafür wird ein Fit durch kleinste Quadrate mit Nebenbedingungen benutzt. Wenn Supersymmetrie existiert und R-Parität erhalten ist, zerfallen alle produzierten Susy-Teilchen direkt oder über eine Kaskade in das leichteste supersymmetrische Teilchen (LSP), das stabil ist und nicht detektiert werden kann. Jedes in der Zerfallskaskade auftauchende massive Teilchen kann für eine Zwangsbedingnung auf die invariante Masse benutzt werden. Mit Hilfe solcher Zwangsbedingungen lassen sich die nicht messbaren Impulsekomponenten der LSPs rekonstruieren.

Die Massen der Susy-Teilchen gehen als Hypothesen in den Fit ein. Durch Scannen der Massen wird der Fit mit verschiedenen Hypothesen wiederholt. Mit dem χ^2 des Fits liegt ein Maß vor, das geeignet ist, gute von schlechten Massenhypothesen zu unterscheiden. Somit kann die Methode genutzt werden, um die Massenparameter zu bestimmen. Die Technik wird vorgestellt anhand des supersymmetrischen Modells mSUGRA. Die Zweige der Signalkaskade sind $\tilde{g} \to \tilde{q} \to \chi_2^0/\chi_1^\pm \to \chi_1^0(\text{LSP})$ und $\tilde{q} \to \chi_2^0/\chi_1^\pm \to \chi_1^0(\text{LSP})$.

Die Herausforderungen sind, die Jets zu selektieren, die zu der Signalkaskade gehören, der kombinatorische Untergrund und der Untergrund durch andere Susy-Ereignisse. Die Studie zeigt, dass kinematischen Fits geeignet sind, um Massenbereiche auszuschließen und Hinweise auf die wahren Massen zu geben.

Contents

1 Introduction **1**

2 The Standard Model and Supersymmetry **3**
2.1 The Standard Model of Elementary Particles 3
2.1.1 Particle Content of the Standard Model 3
2.1.2 Gauge Interactions 5
2.1.3 Higgs Mechanisms 10
2.1.4 Problems of the Standard Model 11
2.2 Supersymmetry 13
2.2.1 Solution of the Problems of the Standard Model 14
2.2.2 Particle Content of Supersymmetric Models 15
2.2.3 Breaking Mechanism of Supersymmetry 16
2.2.4 Experimental Signatures of Supersymmetry 19

3 The LHC and the CMS Experiment **21**
3.1 The Large Hadron Collider 21
3.2 The Compact Muon Solenoid 22
3.2.1 The Tracking System 23
3.2.2 The Electromagnetic Calorimeter 24
3.2.3 The Hadron Calorimeter 25
3.2.4 The Magnet 27
3.2.5 The Muon System 27
3.2.6 The DAQ and the Trigger System 28
3.2.7 The Computing Model 29

4 The Principles of Kinematic Fitting **31**
4.1 Introduction of the Least Square Minimization 31
4.1.1 The Method of Lagrangian Multipliers 32
4.2 Kinematic Fitting of Event Topologies 34
4.2.1 The KinFitter Package 35

5 Kinematic Fits of Supersymmetric Events **37**
5.1 The Signal Sample . . . 37
5.1.1 Signal Selection . . . 39
5.2 The "Truth" Scenario . . . 41
5.2.1 Initial Values . . . 41
5.2.2 χ^2 and χ^2 Probability . . . 42
5.2.3 Mass Scans . . . 47
5.2.4 Simultaneous Scanning of All Involved Susy Masses . . . 52
5.3 The "Realistic" Scenario . . . 57
5.3.1 Selecting the Jets . . . 57
5.3.2 $Z^0/W^{\pm}$ Preselection . . . 57
5.3.3 χ^2 Selection of Combinatorial Hypotheses . . . 59
5.3.4 Fitting with Full Combinatorics . . . 59
5.3.5 Simultaneous Scanning of All Involved Susy Masses . . . 62
5.3.6 Susy Background . . . 66
5.3.7 Signal and Susy Background . . . 71

6 Summary **73**

1 Introduction

A new experiment in high energy physics is going to initiate a new era in understanding the basic concepts of the smallest constituents of matter. In autumn this year the Large Hadron Collider (LHC) at the European Nuclear Research Center (CERN) will be started. Protons with higher energies than in all previous experiments will collide and produce other particles. There are good reasons why theoretical particle physicists expect new particles in these collisions.

The Standard Model of particle physics has described all experimental data of high energy physics experiments till now very precisely, and predicted new particles by considering and requiring symmetry. But some problems emerged. The Standard Model seems not to be the last answer. Many different kinds of extensions of the Standard Model compete to solve its problems.

One of these extensions is Supersymmetry which assumes the symmetry of bosonic and fermionic particles. As stated in the 1960s and 1970s Supersymmetry is the last possible symmetry of space-time which is not experimentally found yet but doesn't conflict with the behavior of elementary particles in collider experiments.

Supersymmetry predicts a lot of new particles: at least one Susy partner for each Standard Model particle. It is one of the main goals of LHC and the detector CMS (Compact Muon Solenoid) to search for these particles. Since Supersymmetry can be realized in different ways and each of these sub-models depends on unknown parameters it is essential to measure the masses of the new particles after Supersymmetry is discovered. Finally, the mass values allow to distinguish between different sub-models and to determine the parameters of this model.

In this study the method of kinematic fits is discussed as one possibility to measure the masses of particles that occur in long decay chains. The fitting technique of constrained least square estimates with Lagrangian Multipliers is performed for different mass hypotheses. Comparing the results of these fits allows a discrimination of the hypotheses and therefore an indirect measurement of the masses.

The data that is used in this study are generated with the Monte Carlo simulation software Pythia assuming the supersymmetric model mSUGRA (minimal Supergravity) with a set of parameters that is called LM4 within the CMS collaboration. Since R-parity is assumed to be conserved, the lightest supersymmetric particle (LSP) is stable. It escapes undetected and therefore its momentum components are unmeasurable parameters which have to be determined by the fit. Each massive intermediate state in

a decay chain is used as a constraint. Since the method only works if there are more constraints than unmeasured parameters, only events with long decay chains are suitable for the kinematic fit.

In such a case however, combinatorial background and background from other processes will be a major challenge.

In chapter 2, a short overview of the basic concepts of the Standard Model of particle physics and the supersymmetric extension is given.

In chapter 3, the accelerator LHC and the detector CMS is described.

In chapter 4, the technique of the kinematic fit using the non-linear constrained least square method with Lagrangian Multipliers is introduced.

In chapter 5, the kinematic fit method is applied to simulated events which are generated assuming Supersymmetry. This is done within two scenarios. In one scenario information from Monte Carlo is used, it is referred to as "truth" scenario. Since this information is not accessible in the real experiment a second scenario is analyzed referred to as "realistic" scenario.

2 The Standard Model and Supersymmetry

2.1 The Standard Model of Elementary Particles

The Standard Model of Elementary Particle Physics describes all known phenomena of High Energy Physics.

In the 1970s the principles of the Standard Model (SM) have been formulated like they are known today. Since then it has been tested precisely without finding any experimental deviation. Besides these many experimental confirmations there is an aesthetic aspect: All fundamental interactions described by the SM derive from one principle, the requirement of local gauge invariance. Quantum chromodynamics (QCD) describes the strong interaction, quantum electrodynamics (QED) describes the electromagnetic interaction and the Glashow-Weinberg-Salam theory combines QED and weak interaction to the electroweak theory. Gravitation is not included in the SM and it is not measurable in present collider experiments since its effect on elementary particles is very small.

The Higgs mechanism is the only part of the SM that is not experimentally confirmed yet. The Higgs boson (or bosons) is responsible for the masses of the particles.

2.1.1 Particle Content of the Standard Model

The Standard Model holds two kinds of particles all matter is made of, leptons and quarks. Both of these are fermions i. e. they have spin 1/2. There are six different leptons and six different quarks grouped into three generations. The stable matter surrounding us is only made of three types of particles: the up u and down d quarks as constituents of all atoms' nuclei and the electrons e^- in the atomic shell.

Besides the electron there are two other similar particles which are much heavier: the muon μ and the tau τ. Muons are produced in a large number in the upper atmosphere where cosmic particles with high energy collide with gas particles.

Each of these leptons has one partner, the neutrino. They only have a small mass compared to their partners and are uncharged. In Tab. 2.1 some properties of the leptons are summarized.

The two types of quarks (called quark flavors) of stable matter belong in the same way to the first and lightest of the three generations of quarks, see Tab. 2.2.

Quark decays within one generation are favored but other decays are possible. In other words: If an up quark emits a W^+ there *always* remains a d', and c decays always into s', and t into b'. But these primed quarks are not exactly the mass eigenstates, they are

	Lepton	Charge/e	Mass/MeV
First generation	electron e	-1	0.511
	ν_e	0	$< 2 \times 10^{-6}$
Second generation	muon μ	-1	106
	ν_μ	0	< 0.2
Third generation	tau τ	-1	1777
	ν_τ	0	< 18

Table 2.1: The leptons of the Standard Model.

	Quark	Charge/e	Mass/MeV
First generation	down d	$-1/3$	2
	up u	$2/3$	5
Second generation	strange s	$-1/3$	100
	charm c	$2/3$	1200
Third generation	bottom b	$-1/3$	4200
	top t	$2/3$	174 000

Table 2.2: The quarks of the Standard Model.

linear combinations mixed by the Kobayashi-Maskawa matrix [1]:

$$\begin{pmatrix} d' \\ s' \\ b' \end{pmatrix} = \begin{pmatrix} 0.974 & 0.227 & 0.004 \\ 0.227 & 0.973 & 0.042 \\ 0.008 & 0.042 & 0.999 \end{pmatrix} \begin{pmatrix} d \\ s \\ b \end{pmatrix} \tag{2.1}$$

The quarks carry an additional charge, called color charge. Each quark is either red, green, or blue, the antiquarks are anti-red, anti-green, or anti-blue. The color is a conserved quantum number.

For all particles carrying color charge a confinement is observed. It states that all free particles are colorless. Therefore quarks constitute hadrons which are color-neutral. This can be achieved by combining for example a red quark with an anti-red antiquark (into a so-called meson) or by combining three quarks carrying all three colors (into a baryon). The latter shows the analogy to visible color: a mixture of red, green, and blue light is perceived as white light.

The interactions are carried by bosonic particles with spin 1. Some properties of these bosons are summarized in Tab. 2.3. The photon γ couples to all electrically charged

Interaction	Boson	Charge/e	Mass/GeV
Strong	8 gluons g	0	0
Electromagnetic	photon γ	0	0
Weak	$W^{\pm}$	± 1	81
	Z^0	0	92

Table 2.3: The gauge bosons of the Standard Model.

particles and transmits the electromagnetic force. The strong interaction is carried by the gluons. They couple to all particles with color charge. Gluons themselves are color charged with one color plus one anti-color. The eight different gluons mentioned in Tab. 2.3 correspond to different combinations of color and anti-color.

2.1.2 Gauge Interactions

All interactions are deduced from the principle of local gauge invariance.

In classical mechanics the Lagrange function is defined as difference of kinetic energy and the potential energy

$$L = T - U. \tag{2.2}$$

The equations of motion are obtained from the Euler-Lagrange equation

$$\frac{d}{dt}\left(\frac{\partial L}{\partial \dot{q}_i}\right) = \frac{\partial L}{\partial q_i} \tag{2.3}$$

The q_i are the coordinates.

This can be adopted to a field theory by replacing the Lagrange function by the Lagrange density, referred to as *Lagrangian* $\mathscr{L}$, and the coordinates by the fields ϕ_i. The derivatives are w. r. t. time and spatial coordinates, written as the vector $x_\mu = (t, x, y, z)$:

$$\partial_\mu \phi_i \equiv \frac{\partial \phi_i}{\partial x^\mu} \tag{2.4}$$

The Euler-Lagrange equation is

$$\partial_\mu \left(\frac{\partial \mathscr{L}}{\partial(\partial_\mu \phi_i)}\right) = \frac{\partial \mathscr{L}}{\partial \phi_i} \tag{2.5}$$

The field of a spin 1/2 particle is written as a Dirac Spinor ψ. The Lagrangian of such a particle with mass m in absence of any interaction is

$$\mathscr{L} = \bar{\psi}(i\gamma^\mu \partial_\mu - m)\psi \tag{2.6}$$

with $\bar{\psi} \equiv \psi^\dagger \gamma^0$. For simplification natural units are used in this thesis where speed of light c and Planck's constant $\hbar$ are set to 1.

The γ matrices originally occurred when Dirac quantized the relativistic energy-momentum relation $p^\mu p_\mu = m^2$ for particles with spin 1/2. He found out that four coefficients γ^0, γ^1, γ^2, and γ^3 are necessary. They have to fulfill the anti-commutator relation

$$\{\gamma^\mu, \gamma^\nu\} = 2g^{\mu\nu} \quad \text{where } g^{\mu\nu} \text{ is the Minkowski metric.} \tag{2.7}$$

This is only possible with matrices which are at least 4×4. The standard Bjorken-Drell convention is:

$$\gamma^0 = \begin{pmatrix} 1 & 0 & 0 & 0 \\ 0 & 1 & 0 & 0 \\ 0 & 0 & -1 & 0 \\ 0 & 0 & 0 & -1 \end{pmatrix} \quad \text{and} \quad \gamma^i = \begin{pmatrix} 0 & \sigma^i \\ -\sigma^i & 0 \end{pmatrix} \tag{2.8}$$

with the three 2×2 Pauli matrices σ^i.

Quantum Electrodynamics

The Dirac equation of a free particle is given by

$$(i\gamma^\mu \partial_\mu - m)\psi(x) = 0 \tag{2.9}$$

The principle of local gauge invariance requires the invariance of the Dirac equation under the transformation

$$\psi \to \psi' = e^{i\theta(x)}\psi \tag{2.10}$$

where $\theta(x)$ is an arbitrary real function in space-time. Putting ψ' into Eq. 2.9 leads to

$$(i\gamma^\mu \partial_\mu - m)\psi'(x) = -\gamma^\mu \partial\theta(x)\psi'(x) = q\gamma^\mu A'_\mu \psi'(x) \tag{2.11}$$

In the last step $A'_\mu = \frac{-1}{q}\partial_\mu \theta(x)$ is introduced to show that this could be read as a Dirac equation of a particle with charge q in an electromagnetic field with 4-potential A'_μ. Performing simultaneously the transformations Eq. 2.10 and

$$A_\mu \to A'_\mu = A_\mu - \frac{1}{q}\partial_\mu \theta(x) \tag{2.12}$$

and replacing the derivative ∂_μ by the covariant derivative $D_\mu = \partial_\mu + iqA_\mu$ finally leads to the required invariance of the Dirac equation $(i\gamma^\mu D_\mu - m)\psi(x) = 0$.

The electromagnetic field is a direct and necessary consequence of the requirement of local gauge invariance of the Dirac equation.

With the electromagnetic field tensor $F_{\mu\nu} = \partial_\mu A_\nu - \partial_\nu A_\mu$ the Lagrangian of a charged fermion within an electromagnetic field can be written as

$$\mathscr{L} = \bar{\psi}(i\gamma^\mu D_\mu - m)\psi - \frac{1}{4}F_{\mu\nu}F^{\mu\nu} \tag{2.13}$$

This gauge transformation with a scalar phase $\theta(x)$ belongs to the unitary group U(1). $e^{i\theta}$ is considered as a unitary 1×1 matrix U where "unitary" means $U^\dagger U = 1$.

Quantum Chromodynamics

In quantum chromodynamics there is not only one charge like in QED but three. Each color is conserved and therefore the Lagrangian has to be invariant under color transformations. The quarks are represented by color triplets of Dirac spinors

$$\psi = \begin{pmatrix} \psi_{\text{red}} \\ \psi_{\text{blue}} \\ \psi_{\text{green}} \end{pmatrix} \tag{2.14}$$

With this ψ vector the Lagrangian looks exactly like in QED:

$$\mathscr{L} = \bar{\psi}(i\gamma^\mu \partial_\mu - m)\psi. \tag{2.15}$$

The local gauge transformation referring to three charges is delivered by a special unitary 3×3 matrix SU where "special" means that the determinant is 1. Such a matrix can be written in terms of the Gell-Mass matrices $\lambda_1 \dots \lambda_8$(see [1], page 287, for example) and eight real parameters $a_1(x) \dots a_8(x)$:

$$SU = e^{i\boldsymbol{\lambda} \cdot \boldsymbol{a}} \tag{2.16}$$

The invariance can be achieved by introducing a covariant derivative

$$D_\mu = \partial_\mu + iq_s \boldsymbol{\lambda} \cdot \boldsymbol{A}_\mu \tag{2.17}$$

where the vector $\boldsymbol{A}_\mu$ contains eight gauge fields. The infinitesimal transformation of $\boldsymbol{A}_\mu$ is given by

$$\boldsymbol{A}_\mu \rightarrow \boldsymbol{A}'_\mu = \boldsymbol{A}_\mu - \partial_\mu \frac{1}{q_s} \boldsymbol{a} - 2(\boldsymbol{a} \times \boldsymbol{A}_\mu) \tag{2.18}$$

The cross product is defined with the structure constant of the $SU(3)$ f_{ijk} by

$$(\boldsymbol{a} \times \boldsymbol{A}_\mu)_i = \sum_{j,k=1}^{8} f_{ijk} a_j A^k_\mu \tag{2.19}$$

The gluon term in the Lagrangian can also be formulated analogue to QED as

$$\mathscr{L}_{\text{gluon}} = -\frac{1}{4} \boldsymbol{F}^{\mu\nu} \cdot \boldsymbol{F}_{\mu\nu} \tag{2.20}$$

with

$$\boldsymbol{F}^{\mu\nu} = \partial^\mu \boldsymbol{A}^\nu - \partial^\nu \boldsymbol{A}^\mu - 2q_s(\boldsymbol{A}^\mu \times \boldsymbol{A}^\nu) \tag{2.21}$$

with the cross product defined in Eq. 2.19.

The complete Lagrangian for the color charged particle in a "color field" is then:

$$\mathscr{L} = \bar{\psi}(i\gamma^\mu \partial_\mu - m)\psi - \frac{1}{4}\boldsymbol{F}^{\mu\nu} \cdot \boldsymbol{F}_{\mu\nu} - (q_s \bar{\psi}\gamma^\mu \boldsymbol{\lambda}\psi)\boldsymbol{A}_\mu \tag{2.22}$$

Using the covariant derivative this equation has exactly the same form as the QED Lagrangian in Eq. 2.13.

Requiring local invariance under the $SU(3)$ transformation leads to eight massless gauge fields representing the eight gluons.

Electroweak Interaction

The weak interaction distinguishes between fermion with positive and fermions with negative chirality. Chirality describes the direction of the spin of a particle relative to the direction of its momentum. For massless particles chirality is the same as helicity h which is the projection of the spin $\boldsymbol{s}$ onto the direction of momentum $\boldsymbol{p}/|\boldsymbol{p}|$:

$$h = \boldsymbol{s} \cdot \frac{\boldsymbol{p}}{|\boldsymbol{p}|} \tag{2.23}$$

A particle with positive helicity ($\boldsymbol{s}$ and $\boldsymbol{p}$ point to the same direction) is called right-handed, a particle with negative helicity ($\boldsymbol{s}$ and $\boldsymbol{p}$ point to opposite directions) is called left-handed.

The chiral states of a Dirac spinor can be written with the $\gamma^5 = i\gamma^0\gamma^1\gamma^2\gamma^3$ matrix:

$$\psi_L = \frac{1}{2}(1 - \gamma^5)\psi \quad \text{and} \quad \psi_R = \frac{1}{2}(1 + \gamma^5)\psi \tag{2.24}$$

The charged-current weak interaction (carried by the $W^\pm$ boson) couples only to left-handed fermions. Therefore these fermions are combined into so called isospin doublets. Isospin is a spin-like quantum number referred to as the charge of the weak interaction. The left-handed fermions have an isospin magnitude of $1/2$ with a third component of $+1/2$ for neutrinos and up-like quarks and $-1/2$ for massive leptons and down-like quarks. The isospin eigenstates of the quarks are the primed ones in Eq. 2.1.

In the interaction term of the Lagrangian only the left-handed projection of the spinor occurs

$$\mathscr{L}_{\text{interaction}} = \frac{1}{2}\bar{\psi}\gamma^\mu(1 - \gamma^5)\psi\boldsymbol{W}_\mu \tag{2.25}$$

with three gauge fields $\boldsymbol{W}_\mu$. This "vector minus axial vector" structure of the coupling causes the parity violation of the weak interaction.

Since there is also the neutral current of weak interaction (carried by the Z^0 boson) the same procedure as in QED and QCD will not lead to a theory which describes the experimental results.

Instead, the Glashow-Salam-Weinberg-Model combines the QED and the weak interaction to one interaction based on a $SU(2) \times U(1)$ symmetry.

The covariant derivative is

$$D_\mu = \partial_\mu - ig'\frac{1}{2}YB_\mu - ig\boldsymbol{T}\boldsymbol{W}_\mu \tag{2.26}$$

Y is the hypercharge, defined by the electric charge q and the third component of the isospin I_3: $Y = 2(q - I_3)$, B_μ is a new U(1) gauge field. The components of the vector $\boldsymbol{T}$ are the Pauli matrices $T_i = \sigma_i/2$.

To complete the Lagrangian we need the field tensors. $B_{\mu\nu}$ is like in QED:

$$B_{\mu\nu} = \partial_\mu B_\nu - \partial_\nu B_\mu. \tag{2.27}$$

$\boldsymbol{W}_{\mu\nu}$ is similar to QCD:

$$\boldsymbol{W}_{\mu\nu} = \partial_\mu \boldsymbol{W}_\nu - \partial_\nu \boldsymbol{W}_\mu - g(\boldsymbol{W}_\mu \times \boldsymbol{W}_\nu) \tag{2.28}$$

Hence, the Lagrangian is

$$\mathscr{L} = \bar{\psi}(i\gamma^\mu D_\mu - m)\psi - \frac{1}{4}\boldsymbol{W}_{\mu\nu}\boldsymbol{W}^{\mu\nu} - \frac{1}{4}B_{\mu\nu}B^{\mu\nu} \tag{2.29}$$

The gauge fields B_μ, W^1_μ, W^2_μ, and W^3_μ are not identical with the particles γ, W^+, W^-, and Z^0. These mass eigenstates are linear combinations of the isospin eigenstates that occur in the Lagrangian in the following way:

$$\begin{pmatrix}\gamma\\ Z^0\end{pmatrix} = \begin{pmatrix}\cos\theta_W & \sin\theta_W\\ -\sin\theta_W & \cos\theta_W\end{pmatrix}\begin{pmatrix}B\\ W^3\end{pmatrix} \tag{2.30}$$

and

$$W^\pm = W^1 \pm iW^2 \tag{2.31}$$

θ_W is referred to as the electroweak mixing angle or Weinberg angle. This parameter also determines the coupling constants in the covariant derivative (Eq. 2.26):

$$g = \frac{e}{\sin\theta_W} \quad \text{and} \quad g' = \frac{e}{\cos\theta_W} \tag{2.32}$$

There are no mass terms for the gauge fields in the Lagrangian of the electroweak interaction (Eq. 2.29). In fact such terms would destroy the invariance of the Lagrangian. It is empirically known that only the photon is massless, $W^\pm$ and Z^0 have masses of nearly 100 GeV.

This discrepancy is solved by a mechanism called "spontaneous symmetry breaking" and therefore the Higgs boson is necessary.

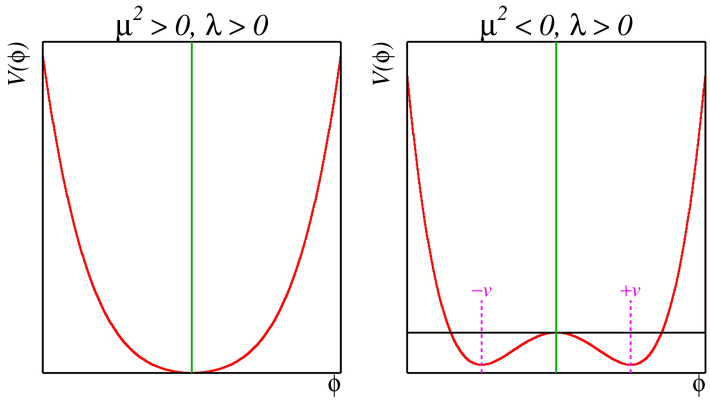

Figure 2.1: Sketch of the Higgs potential in one dimension. Left: The unbroken symmetry for a real μ. Right: If $\mu^2 < 0$ the ground state has not the symmetry of the whole potential [2].

2.1.3 Higgs Mechanisms

The idea of the spontaneous symmetry breaking is to introduce a potential whose ground state doesn't show the symmetry of the potential. In the Higgs mechanism this is realized by a Higgs potential with a non-vanishing vacuum expectation value.

The Higgs potential can be written as [3]:

$$V = \mu^2|\mathbf{\Phi}|^2 + \lambda|\mathbf{\Phi}|^4 \tag{2.33}$$

where $\mathbf{\Phi}$ is a complex isospin doublet

$$\mathbf{\Phi} = \begin{pmatrix} \phi^+ \\ \phi^0 \end{pmatrix} \tag{2.34}$$

If $\mu^2 < 0$ the ground state of V is $|\mathbf{\Phi}|^2 = -1/2\mu^2/\lambda$. Figure 2.1 shows the schematic shape of such a Higgs potential. Introducing the modulus of the vacuum expectation value of $|\Phi|$ as $v/\sqrt{2} = \sqrt{-\mu^2/2\lambda}$ the scalar Higgs doublet with four real fields ξ_1, ξ_2, ξ_3 (written as vector $\boldsymbol{\xi}$), and H can be defined as

$$\Phi = \exp\left(\frac{i\boldsymbol{\xi}\cdot\boldsymbol{\sigma}}{2v}\right)\begin{pmatrix} 0 \\ (v+H)/\sqrt{2} \end{pmatrix}. \tag{2.35}$$

$\boldsymbol{\sigma}$ is the vector of the Pauli matrices.

In this notation the non-vanishing vacuum expectation value is separated and the remaining four real Higgs fields have a vacuum expectation value of zero.

It is possible to get rid of the phase factor in Eq. 2.35 by a gauge transformation. Then, the ξ fields will not appear in the Lagrangian. It can be shown that the degrees of freedom that seem to vanish with the ξ fields reappear in the mass terms of the weak bosons.

The interaction of the electroweak gauge bosons (in terms of the mass eigenstates) with the Higgs field can be written as

$$\mathscr{L} = \frac{1}{2}(\partial H)^2 + \frac{1}{4}g^2 W^+W^-(v+H)^2 + \frac{1}{8}g_Z^2 ZZ(v+H)^2 - V\left[\frac{1}{2}(v+H)^2\right]. \quad (2.36)$$

Expanding this Lagrangian would lead to two terms with v^2 which can be identified as mass terms with the values

$$M_W = \frac{1}{2}gv \quad \text{and} \quad M_Z = \frac{1}{2}g_Z v = \frac{M_W}{\cos\theta_W} \quad (2.37)$$

The fourth real Higgs field H appears as a massive particle in the Lagrangian. This is expected to be the last particle of the Standard Model that is not discovered yet.

Since the Higgs field has been introduced as a field with isospin but without electric charge and color charge only the weak bosons interact with it and get masses while the photon and the gluon stay massless.

The masses of the fermions arise from Yukawa couplings with the Higgs field. Each fermion has a coupling constant proportional to its mass. Therefore a mechanism for the masses is provided but their values remain as free parameters of the model which have to be determined experimentally.

The experimental lower limit on the Standard Model Higgs mass by LEP is 114.4 GeV [4]. A very new result from a combined analysis of the two Tevatron experiments CDF and DØ excludes a narrow band $160 < m_H < 170\,\text{GeV}$ at 95% C. L. [5].

The discovery potential of CMS is split into two mass regions. In the low mass region the $H \to \gamma\gamma$ channel is expected to be dominant. With an integrated luminosity of $30\,\text{fb}^{-1}$ there is expected a $5\,\sigma$ significance for $m_H \lesssim 130\,\text{GeV}$. For higher Higgs masses the $H \to ZZ$ or $H \to WW$ channel becomes important. Already with $10\,\text{fb}^{-1}$ the region $130 \lesssim m_H \lesssim 500\,\text{GeV}$ can be discovered or excluded. With $30\,\text{fb}^{-1}$ this channel is sensitive to $120 \lesssim m_H \lesssim 1\,\text{TeV}$ [6].

2.1.4 Problems of the Standard Model

As outlined in the previous sections the Standard Model of particle physics has been very successful. There is no deviation found in any experiment. Precision measurements at LEP and Tevatron confirmed all predictions.

But nevertheless some issues haven't been solved yet. An obvious problem is that gravitation is not included in the model and that the Higgs boson is not confirmed by

experiments yet. In addition to that there are other problems which will be discussed in detail: The Hierarchy Problem, the problem of Grand Unification, and the problem of Dark Matter.

Hierarchy and Fine-Tuning Problem

The Higgs boson is assumed by the Standard Model to be a scalar spin 0 particle. It is required to couple to all fermions according to their mass. This leads to loop corrections to the mass of the Higgs boson itself as shown in Fig. 2.2.

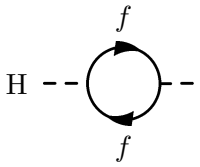

Figure 2.2: Loop corrections to the Higgs mass by fermions

The corrections to the mass parameter μ^2 of the Higgs by such a process is given by

$$\Delta\mu^2 = \frac{|\lambda_f|^2}{16\pi^2}\left(-2\Lambda_{UV}^2 + 6m_f^2 \ln(\Lambda_{UV}/m_f) + \cdots\right) \tag{2.38}$$

where λ_f is the coupling constant of the fermion to the Higgs field and Λ_{UV} is an ultraviolet momentum cutoff. The higher the considered energy scale the higher the cutoff has to be chosen. This cutoff is kind of an upper limit of the energy range in which the theory is valid. Since the loop correction is proportional to the square of this cutoff the Higgs mass diverges with the energy scale. At the Planck's scale for example the correction to μ^2 is about 30 orders of magnitude larger than μ^2 at the electroweak scale itself [7].

Although there is a possibility to cancel the squared divergence within the Standard Model this would require an extreme fine-tuning of some parameters with an accuracy of the order of 10^{-26} in each order of perturbation theory [3].

Neither a strong dependency of the mass of a particle from the energy scale nor an extreme fine-tuning of same parameters is what is expected by a fundamental physical theory.

Grand Unification

Electricity and magnetism have been unified to electromagnetic interaction in the 19^{th} century. In the 1960s the electromagnetic interaction and the weak interaction have been unified to the electroweak interaction. The next step would be the unification with the strong interaction. In such a "Grand Unified Theory" (GUT) all three couplings would be identified as different manifestations of one single interaction.

The hint to this general force are the running coupling constants. While the electromagnetic coupling constant gets larger with the energy scale the strong and the weak coupling constants get smaller. If the inverse coupling constants are plotted over the energy scale they come close to each other at high scales but don't meet at one single point.

Dark Matter

Cosmological observations suggest that about 22% of the content of the universe are the so called Dark Matter [8]. Dark Matter is meant to be not baryonic like stars and dust. Since it is not seen by direct observations this kind of matter doesn't interact electromagnetically. But of course it has to be massive.

The only particles in the Standard Model that are stable and uncharged are the neutrinos. Measurements of solar neutrinos by Super-Kamiokande [9] and the SNO experiment [10] confirm the flavor oscillation of neutrinos which indicates a finite mass.

But nevertheless the mass of the neutrinos is too small to provide the huge amount of Dark Matter that is necessary. In addition to that most of them are highly relativistic which does not agree with the measurements of a halo of cold Dark Matter around the galaxies.

2.2 Supersymmetry

Supersymmetry is the symmetry between fermions and bosons. A transformation operator Q is introduced that combines fermions and bosons:

$$Q\,|\text{boson}\rangle = |\text{fermion}\rangle \quad \text{and reverse.} \tag{2.39}$$

The Coleman-Mandula theorem [11] and the extension by Haag, Łupuszański, and Sohnius [12] state that new symmetries within a quantum field theory are highly restricted. Haag, Łopuszański, and Sohnius actually stated that Supersymmetry is the last possible extension of the Poincare group which does not lead to a trivial scatter matrix [13].

Each particle of the Standard Model becomes part of a supermultiplet with a new particle as superpartner. These partners are suggested to have equal quantum numbers with exception of the spin that differs by 1/2.

This means that the superpartners should have the same mass which is obviously not the case since Supersymmetry is not yet discovered. Consequently the symmetry must be broken.

2.2.1 Solution of the Problems of the Standard Model

Hierarchy Problem

The first problem of the Standard Model mentioned above is the hierarchy problem of the Higgs sector. The assumed new particles which are symmetric to the known fermions but scalar would contribute to the Higgs mass via loops shown in Fig. 2.3

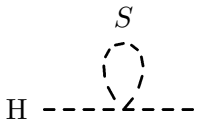

Figure 2.3: Loop corrections to the Higgs mass by scalars

The correction to the Higgs mass is

$$\Delta\mu^2 = \frac{\lambda_S}{16\pi^2}\left(\Lambda_{UV}^2 - 2m_S^2 \ln(\Lambda_{UV}/m_S) + \cdots\right) \tag{2.40}$$

Comparing this contribution with the one from fermions (Eq. 2.38) there is a relative minus sign at the squared cutoff Λ_{UV}. If the coupling constants fulfill $\lambda_S = |\lambda_f|^2$ the divergent contributions would cancel.

Since the masses of superpartners are not equal the coupling constants to the Higgs field are not equal either. But if they don't differ too much ($\lesssim 1\,\text{TeV}$) the corrections are small and the hierarchy problem is solved.

Grand Unification

Seemingly by accident Supersymmetry allows a Grand Unified Theory as well. The new particles contribute to the running couping constants of electromagnetic, weak, and strong interaction and change their slope. Again, if the masses of the Susy particles are $\lesssim 1\,\text{TeV}$ all three coupling constants meet at one single point at a scale of $10^{16}\,\text{GeV}$ as illustrated in Fig. 2.4.

Dark Matter

Within supersymmetric models there is also a solution for the third problem mentioned above. In many sub-models of Supersymmetry the lightest supersymmetric particle (LSP) is stable, massive and only weakly interacting, just as requested for a Dark Matter candidate.

The stability of the LSP is associated with the stability of the proton. In general, the baryon and lepton number conservation can be violated in Supersymmetry without disturbing gauge invariance.

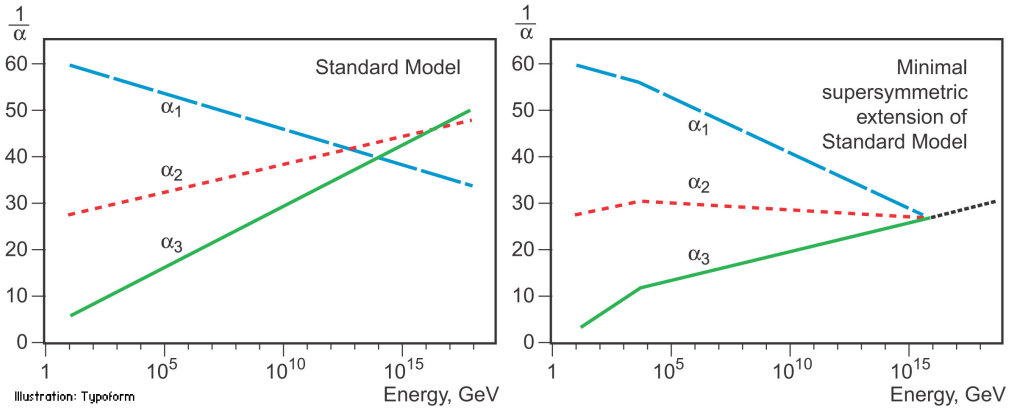

Figure 2.4: Running of the inverse coupling constants: While in the Standard Model the constants miss each other, in Supersymmetry they meet at one point [14].

The experimental lower limit on the proton lifetime is $6.6 \cdot 10^{33}$ years [15]. This is a strong argument why baryon number should also be conserved in Supersymmetry. To achieve this a new quantum number is introduced: the R-parity

$$R = (-1)^{3B+L+2S} \tag{2.41}$$

B is the baryon number, L the lepton number, and S the spin. All Standard Model particles have $R = 1$ while all Susy particles have $R = -1$. The conservation of R would lead to a stable proton and to a stable LSP.

2.2.2 Particle Content of Supersymmetric Models

The number of new particles predicted by a supersymmetric extension is not constant. There are a lot of models possible with different counts of particles. So called Minimal Supersymmetric Standard Models (MSSM) introduce the minimal amount of the particles: one Susy partner for each known particle, except of the Higgs sector where in Supersymmetry two doublets are necessary. One doublet couples to the up-like particles, the other to the down-like particles.

The naming scheme of the Susy particles distinguishes scalars from fermions. The scalars (which are the partners of the Standard Model fermions) get an 's' in front of the Standard Model particle's name: The partner of the quark is called squark, the partner of the lepton is the slepton and so on. The fermionic Susy particles end with 'ino', for example gluino or higgsino. The common notation is a tilde over the symbol. Therefore the selectron for example is written as $\tilde{e}$.

The mass eigenstates of the supersymmetric partners differ from the Standard Model.

The neutral gauginos mix to the four neutralinos $\chi^0_{1\cdots4}$:

$$\begin{pmatrix} \chi^0_1 \\ \chi^0_2 \\ \chi^0_3 \\ \chi^0_4 \end{pmatrix} = \begin{pmatrix} M_1 \cos\theta_W & -M_1 \sin\theta_W & M_Z \sin\theta_W & 0 \\ M_2 \sin\theta_W & M_2 \cos\theta_W & -M_Z \cos\theta_W & 0 \\ 0 & M_Z \cos\beta & -\mu \sin\beta & -\mu \cos\beta \\ 0 & -M_Z \sin\beta & \mu \cos\beta & -\mu \sin\beta \end{pmatrix} \begin{pmatrix} \tilde{\gamma} \\ \tilde{Z}^0 \\ \tilde{H} \\ \tilde{H}' \end{pmatrix} \tag{2.42}$$

The charged gauginos mix to the charginos:

$$\begin{pmatrix} \chi^\pm_1 \\ \chi^\pm_2 \end{pmatrix} = \begin{pmatrix} M_2 & \sqrt{2} M_W \sin\beta \\ \sqrt{2} M_W \cos\beta \sin\theta_W & \mu \end{pmatrix} \begin{pmatrix} \tilde{W}^\pm \\ \tilde{H}^\pm_{u/d} \end{pmatrix} \tag{2.43}$$

M_1 and M_2 are the Susy mass parameters, M_Z and M_W the masses of the Standard Model bosons, and μ is the higgsino mass parameter. θ_W is the electroweak mixing angle and β the ratio of the vacuum expectation values of the Higgs doublets. $\tilde{H}$, $\tilde{H}'$ themselves are mixtures of the neutral up- and down-like higgsinos:

$$\tilde{H} = \tilde{H}^0_u \sin\beta - \tilde{H}^0_d \cos\beta \tag{2.44}$$

$$\tilde{H}' = \tilde{H}^0_u \cos\beta + \tilde{H}^0_d \sin\beta \tag{2.45}$$

In the first step the isospin eigenstate of the electroweak gauge bosons and the Higgs as well as the gauginos and higgsinos mix by electroweak symmetry breaking, in the second step these mixed states mix by Supersymmetry breaking to the listed gauginos χ.

2.2.3 Breaking Mechanism of Supersymmetry

Obviously Supersymmetry is broken. The breaking mechanism for Supersymmetry is not understood yet. The formalism of this breaking is analogue to the electroweak symmetry breaking: The overall Lagrangian should be invariant under Supersymmetry while in the ground state the superpotential doesn't show the symmetry.

The common assumption is that Supersymmetry is broken within a "hidden sector". That means that the fields that cause the breaking (analogue to the Higgs field in the Standard Model) don't have an effect on the physics at low energy scales $\mathcal{O}(1\,\mathrm{TeV})$.

		mass eigenstates
Squarks	$\tilde{u}_L$, $\tilde{u}_R$, $\tilde{d}_L$, $\tilde{d}_R$	the same
	$\tilde{s}_L$, $\tilde{s}_R$, $\tilde{c}_L$, $\tilde{c}_R$	the same
	$\tilde{t}_L$, $\tilde{t}_R$, $\tilde{b}_L$, $\tilde{b}_R$	$\tilde{t}_1$, $\tilde{t}_2$, $\tilde{b}_1$, $\tilde{b}_2$
Sleptons	$\tilde{e}_L$, $\tilde{e}_R$, $\tilde{\nu}_e$	the same
	$\tilde{\mu}_L$, $\tilde{\mu}_R$, $\tilde{\nu}_\mu$	the same
	$\tilde{\tau}_L$, $\tilde{\tau}_R$, $\tilde{\nu}_\tau$	$\tilde{\tau}_1$, $\tilde{\tau}_2$, $\tilde{\nu}_\tau$
Neutralinos	$\tilde{B}^0$, $\tilde{W}^0$, $\tilde{H}_u^0$, $\tilde{H}_d^0$	χ_1^0, χ_2^0, χ_3^0, χ_4^0
Charginos	$\tilde{W}^\pm$, $\tilde{H}_u^+$, $\tilde{H}_d^-$	$\chi_1^\pm$, $\chi_2^\pm$
Gluino	$\tilde{g}$	the same

Table 2.4: New particles of the MSSM

The connection between the hidden sector and the visible physics can be accomplished in different ways. One possibility is that gravitation mediates between the sectors. Such a model is the minimal Supergravity Model (mSUGRA). The huge amount of new parameters that is introduced by Supersymmetry is reduced to five only.

The gauginos have a unified mass parameter at the GUT scale ($m_{1/2}$). Therefore their different masses at low energy scales are no free parameters anymore. They can be calculated by considering all occurring radiative corrections. In the same way all sfermions unify to m_0.

The other free parameters are the ratio of the vacuum expectation values of the two Higgs doublets $\tan\beta = v_u/v_d$, the trilinear coupling A_0 which is also unified at high energy scales, and the sign of the higgsino mass parameter signμ.

Another breaking scenario of Supersymmetry if formulated in gauge-mediated Supersymmetry breaking models (GMSB). Here the gauge interactions of the Standard Model are responsible for the breaking terms in the superpotential.

In this thesis a mSUGRA model is analyzed with a certain set of parameters. Within the CMS collaboration some mSUGRA benchmark points are defined [16]. Those which assume low Susy masses are called LM, those with higher Susy masses are called HM.

In this thesis the point LM4 is used with the parameters

$$\begin{aligned} m_0 &= 210\,\text{GeV} \\ m_{1/2} &= 285\,\text{GeV} \\ \tan\beta &= 10 \\ \mu &> 0 \\ A_0 &= 0 \end{aligned}$$

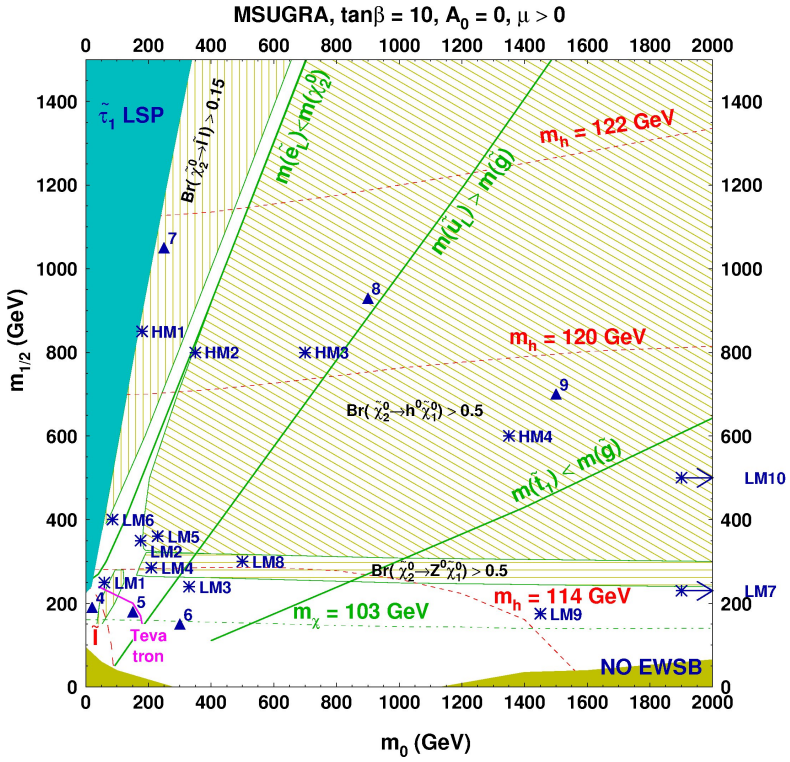

Figure 2.5: The m_0-$m_{1/2}$ plane where the other mSUGRA parameters are constant ($A_0 = 0$, $\tan\beta = 10$, and $\mu > 0$). The CMS benchmark points are marked. The left shaded region is excluded because the charged $\tilde{\tau}$ would be the LSP, the lower shaded area is excluded because the electroweak symmetry breaking would not work. The hatched regions mark different branching ratios of the χ_2^0 as stated in the plot. The green lines separate regions of different mass relations. The exclusion regions reached by Tevatron (magenta) and LEP (red, dashed) are given in the lower left edge [16].

2.2.4 Experimental Signatures of Supersymmetry

All supersymmetric particles are assumed to have high masses compared to the masses of the Standard Model particles. These massive particles have a very short lifetime and decay immediately after they have been produced, of course, except of the LSP if R-parity is conserved. It is not to be expected that these particle can be measured directly. Instead, the decay products have to be analyzed to get information about the decayed particle. This is a common situation well known from measurements of $W^{\pm}$ and Z^0 bosons.

The LSP cannot be detected directly as well. There are strong suggestions that it interacts neither strongly nor electromagnetically. Therefore it will not interact with the material of the detector and vanish unmeasured.

For this reason the main signature of such a Susy model is missing energy. In addition many jets are expected since the Susy particles are produced and decay dominantly via strong interaction in chains with a certain number of supersymmetric intermediate states.

A promising procedure applies cuts on missing transverse energy ($E_T^{\text{miss}} > 200\,\text{GeV}$, for example) and the number of jets ($N_{\text{jets}} > 3$). Some of the jets should have an energy of order 100 GeV. Since jet mismeasurements produce missing energy in QCD events as well, another cut is necessary that rejects events where the direction of the missing energy lies close to the direction of one of the jets with the highest energy. This cut on the azimuth angle ϕ is commonly known as "minimum $\Delta\phi$ cut".

Another variable which seems to be useful to separate Susy signal from Standard Model background is the effective transverse mass, defined as:

$$M_{\text{eff}} = E_T^{\text{miss}} + \sum_{\substack{\text{leading}\\ \text{jets}}} E_T \tag{2.46}$$

where the leading jets are those with the highest transverse energy. M_{eff} is a measure of the masses of the decayed particles and will typically be higher for Susy events than for QCD.

3 The LHC and the CMS Experiment

3.1 The Large Hadron Collider

The Large Hadron Collider (LHC) is a proton-proton-collider operated by the European Organization for Nuclear Research (CERN) near Geneva, Switzerland. It was built in the tunnel of the Large Electron Positron collider (LEP) which was shut down in 2000. The circumference of the LHC is about 27 km. The magnets for focusing and bending the proton beams are superconducting.

The intended energy per proton is 7 TeV, i. e. the center of mass energy will be up to 14 TeV. With 2808 particle bunches (containing about 10^{11} protons each) and a collision frequency of 40 MHz the design luminosity is $L = 10^{34}\,\mathrm{cm}^{-2}\mathrm{s}^{-1}$.

The center of mass energy as well as the luminosity will be much higher compared to the Tevatron, the most powerful hadron collider in the pre-LHC era. The collider at Fermilab, near Chicago, has a center of mass energy of about 2 TeV and a design luminosity of $10^{32}\,\mathrm{cm}^{-2}\mathrm{s}^{-1}$. The higher energy enables the LHC to produce particles in mass regions where new physics is expected. With its high luminosity the LHC can perform precise measurements of the Standard Model as well as searches for new physics.

Due to technical problems with the accelerator a time delay occurred. A few days after the start of the accelerator in September 2008 an electric short-circuit at one dipole bending magnet caused a leak in the cooling system. The suddenly evaporating helium entailed mechanical damage at the magnet and beam pipe. To avoid accidents like this in the future, all magnets have been checked and additional safety systems have been installed. The restart is planned for September 2009 at a reduced energy of 10 TeV for the first hundred pb^{-1}.

There are four main collider experiments at the LHC:

- the multipurpose detector Atlas (A Toroidal LHC Apparatus)
- the multipurpose detector CMS (Compact Muon Solenoid)
- the b physics experiment LHCb (LHC beauty)
- the ion physics experiment Alice (A Large Ion Collider Experiment)[1]

[1] The LHC also runs with heavy ions, so as lead nuclei. The energy will be approximately 3 TeV/nucleon.

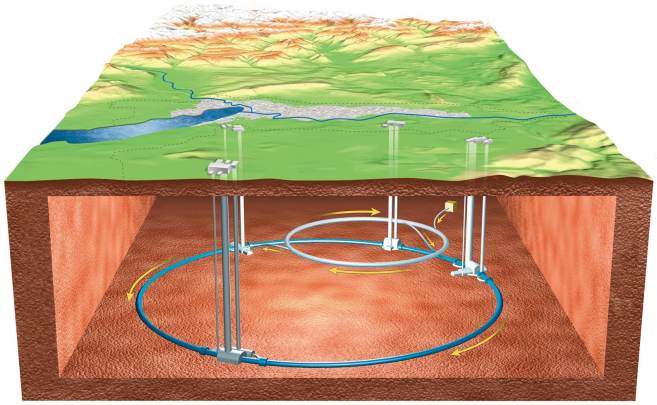

Figure 3.1: The LHC with its experiments: In the front the CMS detector. The other experiments are clockwise: LHCb, Atlas, and Alice. In the back the SPS accelerator that is used as pre-accelerator is shown [17].

The focus of the two multipurpose experiments Atlas and CMS is the finding of the Higgs boson and searching for new physics beyond the Standard Model, such as Supersymmetry. LHCb is specially designed for accurate measurements of the CP-violation which leads to a better understanding of the difference of matter and antimatter. And finally Alice will study quark gluon plasma produced by the collision of heavy ions.

3.2 The Compact Muon Solenoid

The CMS detector is one of the two multipurpose experiments at the LHC. The detector should be able to measure very different kinds of new physics. There are some benchmark channels to test the performance: One of the main goals for CMS is finding the Standard Model Higgs boson. One possible signature is the decay of the Higgs into two photons. For that purpose a very good electromagnetic calorimeter is required. A valid muon identification and momentum resolution is crucial for another signature with a Higgs that decays via $H \rightarrow ZZ \rightarrow e^+e^-\mu^+\mu^-$. This channel has a very clean signature and a relatively small background w. r. t. other processes [16].

The second big challenge is the discovery of new physics like Supersymmetry. This requires a hermetic geometry of the detector to determine E_T^{miss}. Especially the hadron calorimeter is addressed by this request. The energy of all detected particles have to be measured very precisely to avoid failures in determination of E_T^{miss} which is calculated by the transverse momentum balance.

The coordinate system used for CMS has its origin at the nominal collision point in the center of the detector. The y-axis points vertically upward, the x-axis points radi-

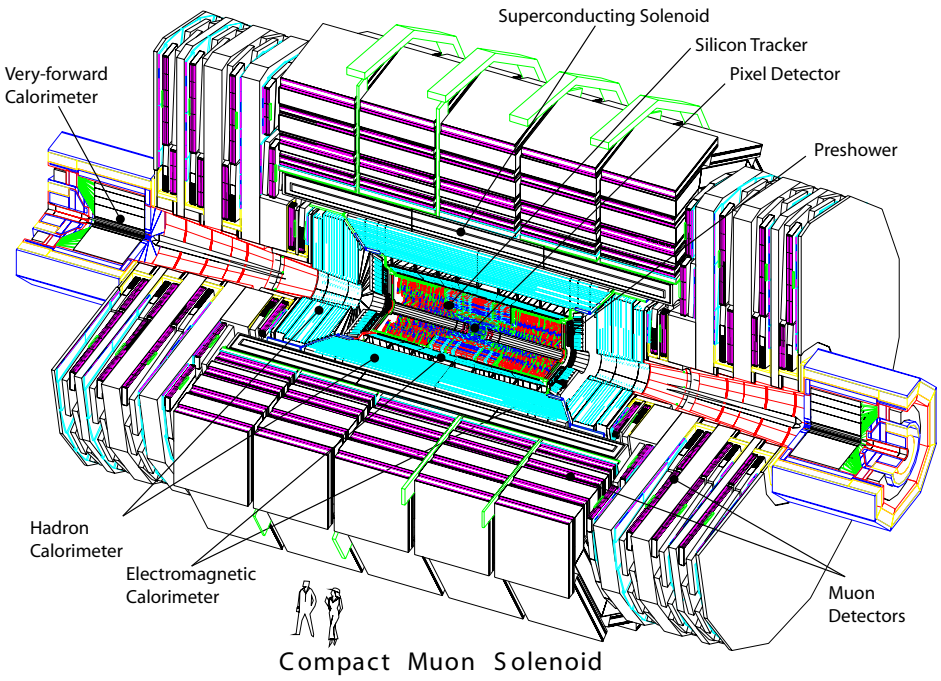

Figure 3.2: A sectional view of the over all CMS detector with its components [18].

ally inward towards the center of the LHC, the z-axis points along the beam line in direction of the Jura. Since the z-component of the initial momentum of the colliding partons in hadron colliders is unknown, the transversal component of the momentum p_T of the final state objects is more useful then its total magnitude. The boost is given in terms of the pseudorapidity η. It is defined as $\eta = -\ln\tan(\theta/2)$, with the polar angle θ measured from the z-axis. For example $\eta = 0$ points orthogonal to the beam line, $\eta = 5$ corresponds to $\theta = 0.77°$.

As usual for modern high energy physics detectors, CMS is built in shells around the crossing point of the beams as shown in the sketch of the detector in Fig. 3.2. In the following the sub-detectors are discussed, beginning with the innermost component.

3.2.1 The Tracking System

The tracker of CMS is the largest silicon detector ever built. It is housed in the tracker support tube which is 5.3 m long, has an inner diameter of 2.38 m, and consists of a silicon pixel and a silicon strip detector.

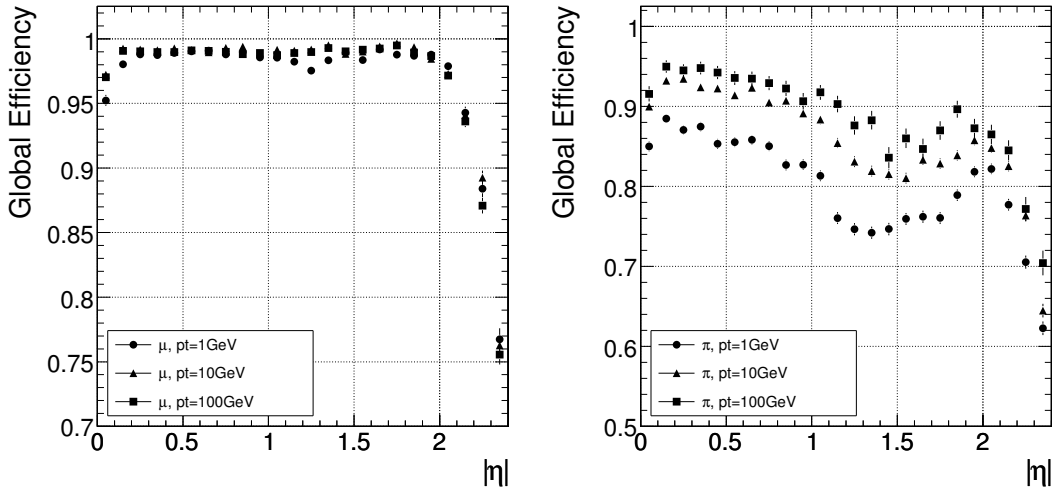

Figure 3.3: Global track efficiencies for muons (left) and pions (right) for different transverse momenta as function of the pseudorapidity η [18].

The silicon pixel detector is placed next to the interaction vertex. It consists of three barrel layers and two endcap disks on each side. The layers have distances of 4.4 cm, 7.3 cm, and 10.2 cm to the beam axis. In total the pixel detector has 66 million pixels. A good resolution as well as a close proximity to the interaction point is necessary to reconstruct the interaction vertex accurately and to measure possible secondary vertexes.

The second tracking module is the silicon microstrip detector. It is located between radius $r = 20\,\text{cm}$ and $r = 55\,\text{cm}$. The inner part, the Tracker Inner Barrel (TIB) is made out of four layers. The strip pitch varies from 80 μm to 120 μm. The Tracker Outer Barrel has six layers with a strip pitch of up to 180 μm.

The endcaps of the tracking system are also divided into two parts: The Tracker Inner Disks (TID) and the Tracker End Cap (TEC). The TEC covers the TOB with nine disks and the three TID fill the gap between the TIB and the TEC.

The efficiency of the whole tracking system is exemplified for muons and pions in Fig. 3.3. All tracker modules have to be aligned very carefully to ensure accuracy of measurement. This means that the true position and orientation of all 15,148 strip and 1440 pixel modules have to be determined on the 10 μm level. This alignment is done with Laser beams as well as with particle tracks.

3.2.2 The Electromagnetic Calorimeter

The purpose of the electromagnetic calorimeter (ECAL) is the energy measurement and identification especially of electrons and photons. It is made out of more than 60,000

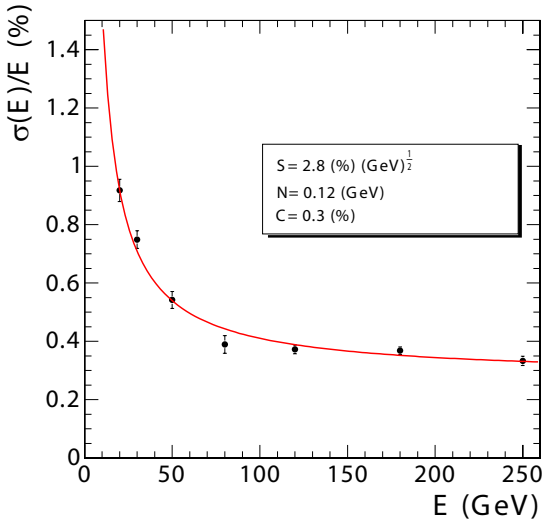

Figure 3.4: The ECAL energy resolution w. r. t. the electron energy. The fitted parameters S, N, and C are explained in the text [18].

lead tungstate ($PbWO_4$) crystals in the barrel region and over 7000 crystals per endcap. This material was chosen because it is suitable for the very compact design of the ECAL inside the solenoid. Other advantages are the fast readout, the fine granularity, and the radiation resistance of the lead tungstate crystals.

The barrel covers up to $|\eta| = 1.479$. One crystal of the barrel part has a front face cross section of about 22 mm × 22 mm and a length of 230 mm, which is equal to about 25 radiation lengths. The resolution of the ECAL measured with an electron test beam is shown in Fig. 3.4. The given numbers in the figure are the stochastic (S), the noise (N) and a constant (C) determined by fitting the measured values to the function

$$\left(\frac{\sigma}{E}\right)^2 = \left(\frac{S}{\sqrt{E}}\right)^2 + \left(\frac{N}{E}\right)^2 + C^2. \tag{3.1}$$

3.2.3 The Hadron Calorimeter

The hadron calorimeter (HCAL) is responsible for measuring the energy of strongly interacting particles. It is located inside the magnet coil. The hermeticity, required for accurate E_T^{miss} measurement, and the minimization of the non-Gaussian tails in the energy resolution are the main requests for the HCAL. It is divided into a hadron barrel (HB), hadron outer (HO), hadron endcaps (HE), and hadron forward (HF). The positions of these components are shown in Fig. 3.5.

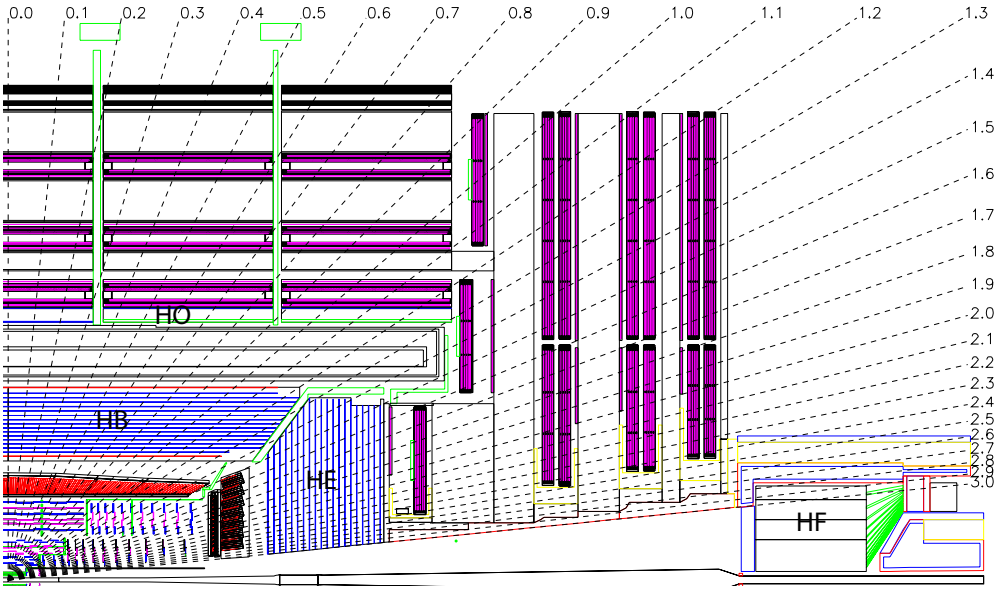

Figure 3.5: Sketch of the HCAL components. In the left lower edge is the crossing point of the beams. The dashed lines give the pseudorapidity η. The muon system is magenta [18].

The hadron barrel covers the pseudorapidity region $|\eta| < 1.4$ with a segmentation of $\Delta\eta \times \Delta\phi = 0.087 \times 0.087$. It is made out of 17 active plastic scintillator tiles. As absorbers 15 brass plates are used, each with a thickness of 5 cm. Brass is a proper material since it has a short interaction length, is easy to manufacture, and is non-magnetic. The amount of absorbing material that can be placed inside the coil is limited. Therefore, as a "tail catcher" the hadron outer encases the solenoid.

The HO consists of scintillators with a thickness of 10 mm. The first layer of the iron return yoke is used as absorber. It is comprising five rings each 2.5 m long in z-direction. The hadron endcaps close on both ends up to $|\eta| < 3$. They consist of 14 η towers with a 5° ϕ segmentation. The hadron calorimeter part next to the beam pipe is the hadron forward (HF) calorimeter. The distance from the front end to the interaction point is about 11 m, the maximal measurable pseudorapidity is 5. It is exposed to a huge flux of particles. Per proton-proton interaction 760 GeV is deposited in the HF on average. As a very radiation hard detector a steel/quartz fiber calorimeter has been chosen. The quartz fibers are placed 5 mm apart in a square grid running parallel to the beam pipe.

The resolution of the whole hadron calorimeter of measured jets is plotted in Fig. 3.6. The resolution of missing transverse energy in QCD dijet events with pile-up is

$$\sigma(E_T^{\text{miss}}) \approx \sqrt{\sum E_T}. \tag{3.2}$$

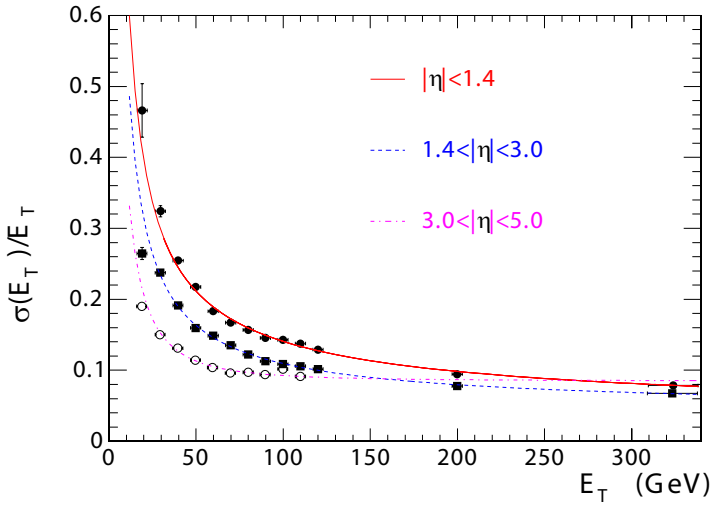

Figure 3.6: Resolution of the transverse energy of jet measurement w. r. t. the momentum for different detector regions [18].

3.2.4 The Magnet

The big superconducting solenoid is located between the HB and the HO. Its radius is about 2.9 m, the length nearly 13 m. The field strength is 4 T caused by a circulating current of 19.5 kA. The motivation for this high magnetic field is the ability to measure high track momenta accurately, and for example the sign of charge of a muon with an energy up to 1 TeV.

3.2.5 The Muon System

The measurement of muons is one of the main tasks of the CMS experiment. These minimal ionizing particles cross the inner detector components without depositing much energy and reach the outermost part of the detector, the muon system.

In the barrel region the muon system consists of drift tube chambers within the iron return yoke of the magnet. Because of the high magnetic field and the high rate of muons and the neutron induced background, another technology has to be chosen for the endcaps. Cathode strip chambers are installed here. They reach close to the beam pipe up to a pseudorapidity of 2.4. In both regions, barrel and endcap, there are additional resistive plate chambers which are characterized by a fast response and a good time resolution. This is necessary since the muons are used by the trigger system as well.

The final momentum resolution of the muons is increased by the combination of the muon system and the inner tracker as shown in Fig. 3.7.

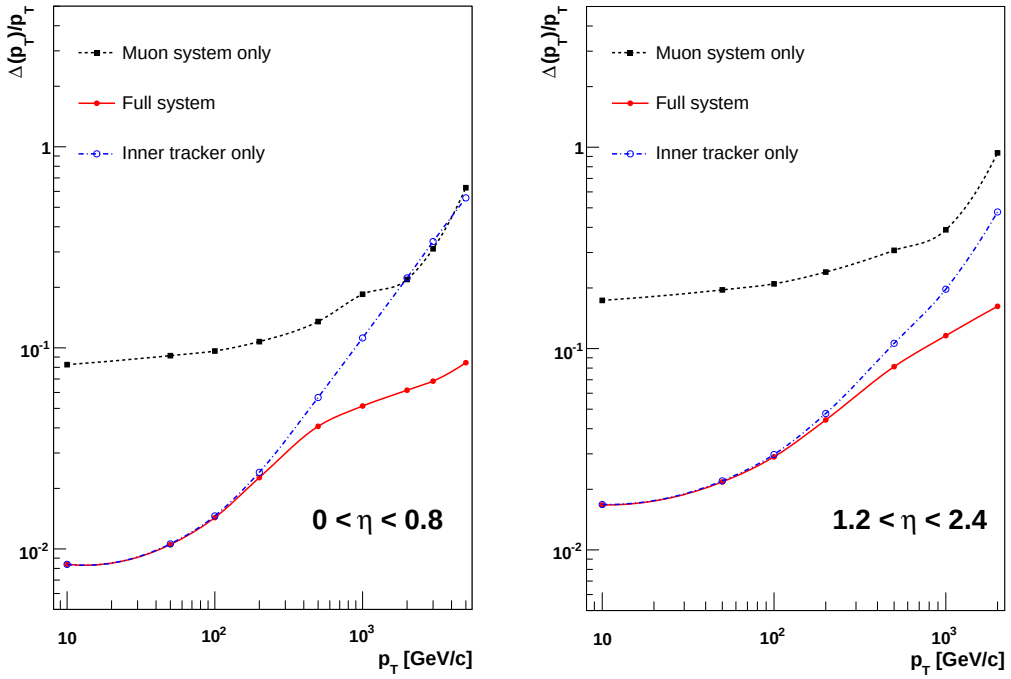

Figure 3.7: The resolution of the muon momentum measurement w. r. t. the momentum for the muon system only, the tracker system only, and both systems combined. Left: in the barrel region, right: in the endcap region [18].

3.2.6 The DAQ and the Trigger System

Caused by the high luminosity and the short interval between two bunch crossings of 25 ns a huge amount of data is produced that is impossible to store. About 10^9 interactions per second are expected at design luminosity. An effective data acquisition (DAQ) and trigger system is necessary, since only 10^2 of these can be stored. This system consists of four parts: the detector electronics, the Level-1 trigger, the readout network, and the online event filter system which runs the High-Level Triggers (HLT). The Level-1 trigger has to make its decision if an event is taken or rejected within 3.2 µs. It involves the calorimeters and the muon system. An event is accepted if some p_T or E_T thresholds are passed by objects like photons, electrons, muons, and jets. Also the sums of E_T and E_T^{miss} are considered for decision. The outcome is still 10^5 events per second which are transfered to the HLT.

The HLT has access to the complete read-out data. On a filter farm of about one

thousand commercial processors, complex calculations similar to those made in off-line analysis are made to decide if an event is of interest. This can take up to 1 second per event and leads to the HLT output rate of 100 events per second.

3.2.7 The Computing Model

The CMS computing system has to handle this still huge amount of data. Is is responsible for storage, access, reconstruction, and analysis of the data. The computing system is decentralized, based on one so called "Tier-0" center at CERN and multiple "Tier-1" and "Tier-2" centers at laboratories and universities worldwide. A computing grid allows for usage of the data by the physicists.

Tier-0 stores all raw data from the DAQ system and performs a first reconstruction of physical objects out of it. Both the raw and the so called RECO data are copied to the Tier-1 centers. The Tier-0 is not accessible for user analyses.

At each Tier-1 a fraction of the complete CMS data is kept in storage. These centers provide the data for the Tier-2 centers.

Tier-2 centers are designed to support many kinds of physics analysis needing only a reduced dataset.

4 The Principles of Kinematic Fitting

4.1 Introduction of the Least Square Minimization

In this study the least square method is used. It is suitable to compare data, i.e. measured values with the prediction of a model. The sum of the squared normalized deviations of the data from the model quantifies the agreement of the data with the model. The measured values are elements of the vector $\boldsymbol{y}$. The predictions of the model, referred to as true values, get the symbol $\bar{\boldsymbol{y}}$. In addition there can be other model parameters which can not be measured. They are labeled with $\boldsymbol{a}$. $\bar{\boldsymbol{y}}$ is the result of the model equations

$$\begin{aligned} f_1(\bar{\boldsymbol{y}}, \boldsymbol{a}) &= 0 \\ f_2(\bar{\boldsymbol{y}}, \boldsymbol{a}) &= 0 \\ &\vdots \\ f_m(\bar{\boldsymbol{y}}, \boldsymbol{a}) &= 0 \end{aligned} \tag{4.1}$$

In this notation $\Delta\boldsymbol{y} = \bar{\boldsymbol{y}} - \boldsymbol{y}$ is the vector of the deviations, also called residuals, and S is the sum of the squared residuals:

$$S = \sum_{i=1}^{n} \Delta y_i^2. \tag{4.2}$$

A very simple case is a model that predicts a straight line as the correlation between two variables y_1 and y_2:

$$f_1 : \quad y_1 - a_1 y_2 - a_2 = 0 \tag{4.3}$$

y_1 and y_2 can be measured, a_1 and a_2 can be quantified by minimizing S. Obviously at least three measured pairs (y_1, y_2) are needed, because two pairs will always fulfill Eq. 4.3 exactly and $S = 0$. Only in an over-determined system, S is suitable to assess if the data conforms to the model.

Since all measurements contain uncertainties, definition 4.2 can be changed to

$$S = \Delta\boldsymbol{y}^T \boldsymbol{V}^{-1} \Delta\boldsymbol{y}, \tag{4.4}$$

where $\boldsymbol{V}$ is the covariance matrix. $\boldsymbol{V}$ consists of the squared errors σ_i^2 of each y_i in the diagonal and the correlations between y_i and y_j in the form of $\rho_{ij}\ \sigma_i\sigma_j$ as off-diagonal elements. The measured values are assumed to be Gaussian distributed.

If all measurements have the same error σ the expectation of S only depends on this error and the difference of the number of measurements n and the number of parameters p:

$$E[S] = \sigma^2(n-p) \tag{4.5}$$

A very important property of the least square method is, that the solution is unbiased if the data is unbiased. The expectation of the parameters are their true values:

$$E[\boldsymbol{a}] = \bar{\boldsymbol{a}} \tag{4.6}$$

The Gauss-Markoff-Theorem states that the error of the parameters estimated with least square method is as small as possible compared to all other techniques of parameter estimation [19].

4.1.1 The Method of Lagrangian Multipliers

A general way to minimize a multi-dimensional system under several constraints like Eq. 4.1 is the method of the Lagrangian Multipliers [20]. For each constraint one additional parameter λ_k is introduced. The minimization of Eq. 4.4 changes into the search for the stationary point of

$$L(\boldsymbol{y}) = S(\boldsymbol{y}) + 2\sum_{k=1}^{m} \lambda_k f_k(\boldsymbol{y}, \boldsymbol{a}) \tag{4.7}$$

Both expressions are equivalent if the constraints are fulfilled exactly.

In the case of linear constraints the solution can be calculated in one step. Non-linear problems need to be solved by an iterative Newton approach: The constraints have to be linearized at chosen initial values to get a first approximation. At this approximation the constraints are linearized again to calculate the next one and iteratively as many times as necessary. In the following this approximative solution is written in terms of corrections to the initial values.

The procedure starts with the measured values $\boldsymbol{y}$ and a good choice of initial values for the parameters $\boldsymbol{a}$. The non-linear constraints are replaced by their first order Taylor expansion.

$$f_k(\boldsymbol{a}^*, \boldsymbol{y}^*) + \sum_{j=1}^{p} \frac{\partial f_k}{\partial a_j}(\Delta a_j - \Delta a_j^*) + \sum_{i=1}^{n} \frac{\partial f_k}{\partial y_j}(\Delta y_i - \Delta y_i^*) \approx 0 \tag{4.8}$$

The $*$ denotes the values after the preceding iteration, or the initial values in the first iteration. $\Delta\boldsymbol{y}^*$ is the correction of the preceding iteration $\Delta\boldsymbol{y}^* = \boldsymbol{y}^* - \boldsymbol{y}$, and similar for

$\Delta \boldsymbol{a}^*$. Using vector notation this is:

$$\boldsymbol{f}^* + \boldsymbol{A}(\Delta \boldsymbol{a} - \Delta \boldsymbol{a}^*) + \boldsymbol{B}(\Delta \boldsymbol{y} - \Delta \boldsymbol{y}^*) \approx 0 \tag{4.9}$$

with

$$\boldsymbol{f}^* = \begin{pmatrix} f_1(\boldsymbol{a}^*, \boldsymbol{y}^*) \\ f_2(\boldsymbol{a}^*, \boldsymbol{y}^*) \\ \vdots \\ f_m(\boldsymbol{a}^*, \boldsymbol{y}^*) \end{pmatrix} \tag{4.10}$$

and $\boldsymbol{A}$ and $\boldsymbol{B}$ are the Jacobi matrices of the unmeasured and the measured variables, respectively.

$$\boldsymbol{A} = \begin{pmatrix} \partial f_1/\partial a_1 & \partial f_1/\partial a_2 & \cdots & \partial f_1/\partial a_p \\ \partial f_2/\partial a_1 & \partial f_2/\partial a_2 & \cdots & \partial f_2/\partial a_p \\ \vdots & \vdots & \ddots & \vdots \\ \partial f_m/\partial a_1 & \partial f_m/\partial a_2 & \cdots & \partial f_m/\partial a_p \end{pmatrix} \tag{4.11}$$

$$\boldsymbol{B} = \begin{pmatrix} \partial f_1/\partial y_1 & \partial f_1/\partial y_2 & \cdots & \partial f_1/\partial y_n \\ \partial f_2/\partial y_1 & \partial f_2/\partial y_2 & \cdots & \partial f_2/\partial y_n \\ \vdots & \vdots & \ddots & \vdots \\ \partial f_m/\partial y_1 & \partial f_m/\partial y_2 & \cdots & \partial f_m/\partial y_n \end{pmatrix} \tag{4.12}$$

Another rewriting of Eq. 4.9 separates the values marked with $*$:

$$\boldsymbol{A}\Delta \boldsymbol{a} + \boldsymbol{B}\Delta \boldsymbol{y} = \boldsymbol{c} \qquad \text{with} \quad \boldsymbol{c} = \boldsymbol{A}\Delta \boldsymbol{a}^* + \boldsymbol{B}\Delta \boldsymbol{y}^* - \boldsymbol{f}^* \tag{4.13}$$

Equation 4.7 becomes in vector notation

$$L = \Delta \boldsymbol{y}^T \boldsymbol{V}^{-1} \Delta \boldsymbol{y} + 2\boldsymbol{\lambda}^T (\boldsymbol{A}\Delta \boldsymbol{a} + \boldsymbol{B}\Delta \boldsymbol{y} - \boldsymbol{c}) \tag{4.14}$$

Differentiation by $\boldsymbol{\Delta y}$, $\boldsymbol{\Delta a}$ and $\boldsymbol{\lambda}$ leads to three conditions of local extrema:

$$\begin{array}{rcrl} \boldsymbol{V}^{-1}\boldsymbol{\Delta y} & & + \; \boldsymbol{B}^T\boldsymbol{\lambda} & = 0 \\ & & \boldsymbol{A}^T\boldsymbol{\lambda} & = 0 \\ \boldsymbol{B}\boldsymbol{\Delta y} & + \; \boldsymbol{A}\boldsymbol{\Delta a} & & = \boldsymbol{c} \end{array} \tag{4.15}$$

or in matrix notation:

$$\begin{pmatrix} \boldsymbol{V}^{-1} & 0 & \boldsymbol{B}^T \\ 0 & 0 & \boldsymbol{A}^T \\ \boldsymbol{B} & \boldsymbol{A} & 0 \end{pmatrix} \begin{pmatrix} \boldsymbol{\Delta y} \\ \boldsymbol{\Delta a} \\ \boldsymbol{\lambda} \end{pmatrix} = \begin{pmatrix} 0 \\ 0 \\ \boldsymbol{c} \end{pmatrix} \tag{4.16}$$

In matrix notations it is obvious that the corrections in each iteration are calculated by inverting the matrix. The sub-matrix $\boldsymbol{V}^{-1}$ has as many rows and columns as measured values are dealt with, namely n. $\boldsymbol{B}$ is a $n \times m$ matrix, and $\boldsymbol{A}$ is a $p \times m$ matrix with the number of measurements n, number of constraints m, and the number of parameters p. So one has to invert a $(n + p + m) \times (n + p + m)$ matrix.

To handle non linear problems, there has to be a convergence criterion, when the iteration shall stop. Two different numbers take part in this criterion. One is the sum of the absolute values of all constraints (Eqs. 4.1) which should be below a certain threshold ϵ_F. The other is ΔS (the change of S from one iteration step to the next) which should be small in the minimum of the χ^2 potential.

$$F = \sum_k |f_k(\boldsymbol{a} + \Delta\boldsymbol{a}, \boldsymbol{y} + \Delta\boldsymbol{y})| < \epsilon_F \tag{4.17}$$

$$\Delta S < \epsilon_S \tag{4.18}$$

If the model is correct, the measurements are Gaussian and unbiased and if the constraints are linear, S behaves like a χ^2 distribution with $m - p$ degrees of freedom. In the following it is assumed that the Taylor approximations of the constraints are very close to their true (non-linear) function in the minimum of the χ^2 potential. In this case the final S of the fit which is the minimum can be interpreted as a χ^2 with $m - p$ degrees of freedom.

4.2 Kinematic Fitting of Event Topologies

For many experiments in high energy physics the kinematic fit method is applied to event topologies. An example from LEP are improvements of the measurement of the W mass [21]. At BaBar (an experiment at the Stanford Linear Accelerator Center (SLAC)) the technique was used in B physics [22].

The measured values in particle physics events are the 4-vectors of the objects measured by the detector. Since we assume R-parity conservation, there are two LSPs and therefore unmeasured values in each supersymmetric event, too. The constraints are the invariant masses on one hand and the p_T balance on the other. The process shown in Fig. 4.1 would be described by the following constraints:

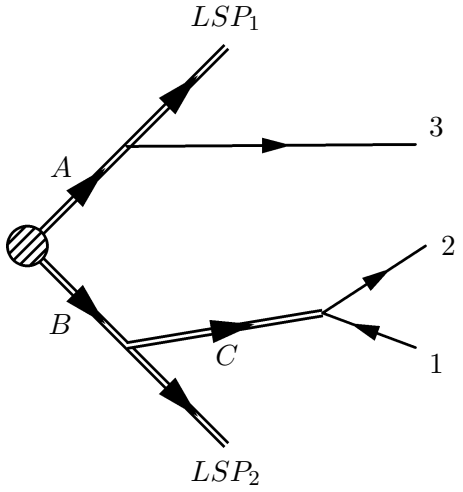

Figure 4.1: A scheme of an event with three decaying massive particles (A, B, and C) and five final state particles: two stable but unmeasurable massive particles (LSP_1 and LSP_2), and three measurable particles (1, 2, and 3).

$$f_{\text{mass}}: \quad (P_3 + P_{LSP1})^2 - M_A^2 = 0 \tag{4.19}$$

$$(P_1 + P_2 + P_{LSP2})^2 - M_B^2 = 0 \tag{4.20}$$

$$(P_1 + P_2)^2 - M_C^2 = 0 \tag{4.21}$$

$$f_{p_T \text{ balance}}: \quad \sum_{\text{all final state objects}} p_x = 0 \tag{4.22}$$

$$\sum_{\text{all final state objects}} p_y = 0 \tag{4.23}$$

There are three massive particles A, B, and C, three measurable final state objects 1, 2, and 3, and two unmeasurable LSPs. If all particle masses are assumed to be known, only the LSPs' momenta components are unknown. So one ends up with six unknowns and five equations. The system is under-constrained, and a least square fit would not make sense. A larger decay chain will solve this problem. Each massive particle in the cascade contributes one mass constraint. That means at least two more particles are necessary to make the system over-constrained.

4.2.1 The KinFitter Package

In this study the KinFitter Package [23] is used. It is a special software for fitting event topologies in high energy physics. The software was originally developed in Fortran for the ALEPH Collaboration and called ABCFIT [24]. A C++ version named KinFitter exists since 2004 within the CMS framework.

The KinFitter provides different parameterizations of particles or jets and different types of constraints. The final objects in the process can be parametrized in different coordinates, like Cartesian, spherical, or the variables often used in hadron colliders: the transverse energy E_T, the pseudorapidity η, and the azimuth angle ϕ. Another difference in the parametrization is the number of free parameters per final state. There are the three free momentum parameters for particles with a fixed mass, as well as for jets which are assumed to be massless.

KinFitter supports two kinds of constraints: mass constraints on one hand and p_T balance constraints on the other.

The KinFitter calculates the two Jacobi matrices $\boldsymbol{A}$ and $\boldsymbol{B}$ (Eqs. 4.11 and 4.12) and the values of the constraints $\boldsymbol{f}^*$ (Eq. 4.10) in each iteration.

The mass constraints are formulated as Gaussian constraints to take the width of masses of particles with a short lifetime into account. These constraints are not handled with the pure method of Lagrangian Multipliers but contribute to the χ^2 term S (Eq. 4.4) with the deviation of the mean of the Gaussian and its width σ. The constraint function f is not $M_{\text{invariant}} - M_{\text{constraint}} = 0$ anymore but becomes the form of

$$M_{\text{invariant}} - \alpha M_{\text{constraint}} = 0. \tag{4.24}$$

with the new parameter α.

Convergence Criteria

Since the problem is solved iteratively, a criterion has to be defined that stops the iteration. ΔS is the difference of the χ^2 term S from one iteration to the next. It is expected that this change ΔS should be small in the minimum of the χ^2 potential. The value depends on the problem. Since S is normalized $\Delta S = 1$ is equivalent to $1\,\sigma$. In this study this convergence criterion is set to $\Delta S \leq 0.1$ which means that the change of S is small compared to the errors of the parameters.

Of course we are only interested in minima where the constraints are fulfilled. Consequently a second criterion is $\sum f \leq 0.1$. Again, this value depends on the problem. These two criteria have to be fulfilled simultaneously to accept the calculation as converged.

To prevent the procedure from infinite loops a maximum number of allowed iterations is set. The procedure stops when this number of iterations is reached although the convergence criteria are not fulfilled. In this case the event is referred to as not converged. This maximum number of iterations has to be chosen carefully. If it is too small some events don't reach the minimum although they eventually would. If it is too large computing time increases unnecessarily caused by events which don't converge at all. It turned out that 20 iterations are just enough for the dedicated problem.

5 Kinematic Fits of Supersymmetric Events

In this chapter the technique of kinematic fits is applied to supersymmetric events. There are several measured and several unmeasured values in each event. The measured values are energy and momentum of final state objects so as jets. The unmeasured values are unmeasurable final state objects so as the LSP. The masses of the intermediate particles and the transverse momentum balance are used as constraints.

The kinematic fit can determine the LSP momenta if the system is over-constrained. Therefore one has to assume a hypothesis for the masses of the supersymmetric particles. The fit is performed for different mass hypotheses and the resulting χ^2 is used to discriminate good hypotheses from bad hypotheses. This allows an indirect measurement of the mass parameters.

In section 5.2 the procedure is applied within a "truth" scenario. The principle capability of the method is shown there. After that the scenario is modified to a more "realistic" setting in section 5.3. There it is shown whether the method still works under conditions which approach the situation with real measured data.

5.1 The Signal Sample

The Monte Carlo simulated data this study deals with, is a Pythia simulated sample at the mSUGRA test point LM4. Within mSUGRA there are only five additional parameters for the supersymmetric particles as discussed in chapter 2. In the CMS collaboration, different test points have been defined. LM4 is one of the low mass points just beyond the Tevatron reach with the following parameters:

- $M_0 = 210\,\mathrm{GeV}$
- $M_{1/2} = 285\,\mathrm{GeV}$
- $\tan\beta = 10$
- $sgn(\mu) = +$
- $A_0 = 0$

The total cross section of mSUGRA at LM4 in leading order is 19.4 pb.

A kinematic fit for each single event requires an over-determined system. Since R-parity is assumed to be conserved, supersymmetric particles are produced pairwise and

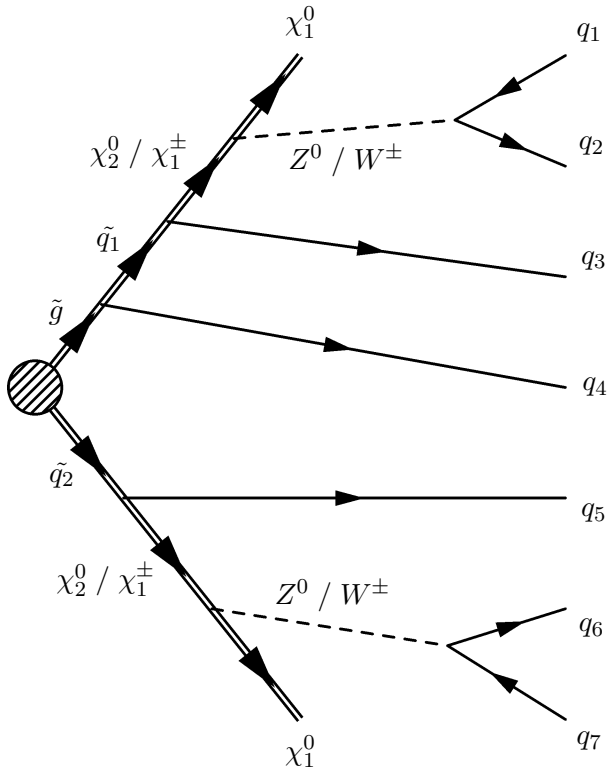

Figure 5.1: Feynman diagram of the signal cascade this study deals with.

Susy particles don't decay into Standard Model particles only. So if supersymmetric particles are produced there are at least two of them, and each one decays finally into the lightest Susy particle (LSP) which has to be stable. This leads to six unmeasured variables in each event, the three momentum parameters per LSP.

In order to have an over-determined system at least seven constraints are required. This sets a lower limit on the length of the decay chain for which this method can be applied (see chapter 4). Since there are two constraints from p_T balance one needs two decay chains with at least five intermediate Susy particles in total. Considering this, the cascade with the highest abundance is shown in Fig. 5.1. Because of the higher branching ratio this study is done in the all-hadronic channel, i. e. without any leptons. Although lepton measurements are more precise and the combinatorial problem (described later) would be reduced.

The masses of the neutralino χ_2^0 and the chargino $\chi_1^\pm$ are almost the same at the tested mSUGRA parameter point. Therefore one mass constraint can be used for both.

The masses of the different squark flavors are not exactly degenerated. To get to an acceptable situation only left-handed up, down, strange, and charm squarks are accepted in the signal sample. Their masses lie in a quite narrow region, they differ by about 0.4%.

The right-handed squarks don't appear in such an event topology at all since they decay at LM4 with almost 100% directly into the LSP χ_1^0.

The sparticle masses occurring in this cascade at the electroweak scale are:

- $M(\tilde{g}) = 715\,\text{GeV}$
- $M(\tilde{u}_L) \approx M(\tilde{d}_L) \approx M(\tilde{s}_L) \approx M(\tilde{c}_L) \approx 646\,\text{GeV}$
- $M(\chi_2^0) \approx M(\chi_1^\pm) \approx 217\,\text{GeV}$
- $M(\chi_1^0) = 114.5\,\text{GeV}$

The cross section of $\tilde{g}\,\tilde{q}$ production at this test point is about 4.4 pb. About 16% of the gluinos decay into left-handed squarks. Others decay into right-handed squarks and into the light $\tilde{t}$ and $\tilde{b}$. The left-handed squarks decay almost completely into either χ_2^0 or $\chi_1^\pm$. Again, almost 100% of the gauginos χ_2^0 and $\chi_1^\pm$ decay into $\chi_1^0\,Z^0$ and $\chi_1^0\,W^\pm$, respectivly. The Standard Model bosons decay in about two thirds of all cases hadronically.

In summary about 8% of the produced $\tilde{g}\,\tilde{q}_L$ pairs decay according to the cascade in Fig. 5.1.

The Monte Carlo sample contains 92 494 events which corresponds to an integrated luminosity of $L = 3.6\,\text{fb}^{-1}$. 1639 of these contain the cascade that is searched for.

5.1.1 Signal Selection

At first a ΔR matching between the generated partons and the reconstructed jets is performed for the 1639 cascade events. ΔR is the angular distance in ϕ and η: $\Delta R = \sqrt{\Delta\phi^2 + \Delta\eta^2}$. The ΔR between the generated parton and the reconstructed jet has to be less than 0.3. The matching requires a "one-to-one" linking: Each parton has to be matched to one single jet, and each jet has to be matched to one single parton. For 356 events the matching is successful. For all other events at least one parton cannot be matched to a jet. One reason for a failed matching is an incorrectly reconstructed jet. This happens for example if the transverse momentum is very low or if the jet direction is close to the beamline. Another reason is final state radiation. Due to the radiation the direction of the parton is changed and therefore the jet direction doesn't fit to the primary direction of the parton.

In addition one parton from initial state radiation (ISR) is matched to a jet if possible. This ensures that the system of jets which are selected for the fit together with the unmeasured LSPs is balanced in transverse momentum p_T. If there is more than one ISR parton, the leading parton in p_T is used. This matching is not a requirement. If no matching jet is found the initial state radiation will be ignored in the fit.

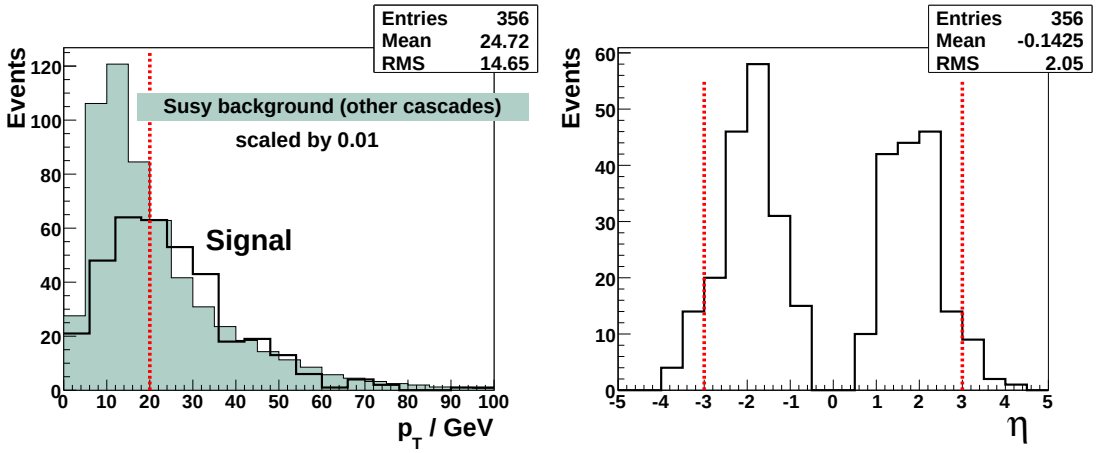

Figure 5.2: Left: p_T of the matched cascade jet with the smallest p_T. For the Susy background from other cascades the seventh hardest jet is taken. It is scaled down by a factor 100. Right: η of the matched cascade jet with the largest η. The red lines mark the cuts of the pre-selection.

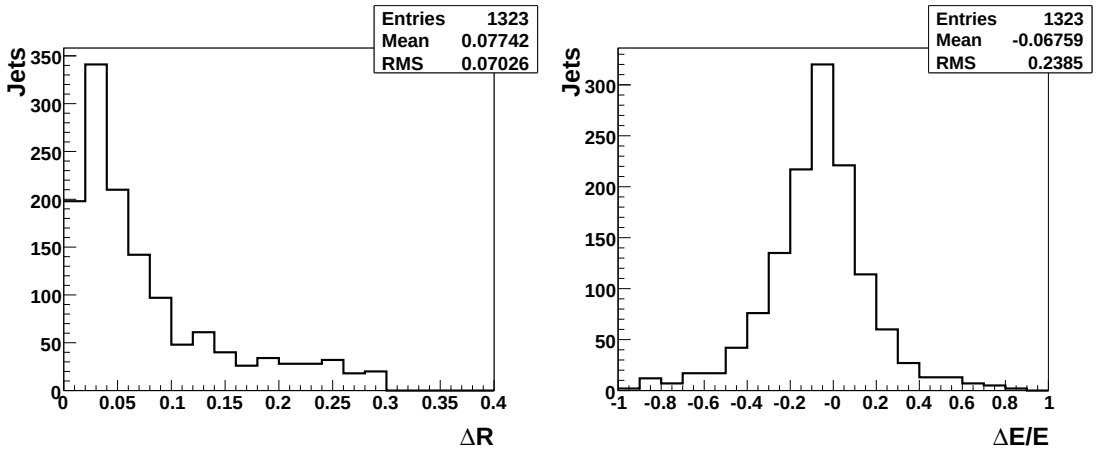

Figure 5.3: Control plots for the jet matching. Left: ΔR between the reconstructed and corrected jet and the matched parton, right: the relative difference in energy.

Then two pre-selection cuts are applied. The transverse momentum p_T of the jets in the cascade has to be at least 20 GeV, their pseudo-rapidity η has to be smaller than 3. The initial state radiation is neglected if the matched jet lies outside these cuts. Figure 5.2 shows the distribution of the corresponding variables with the applied cuts. Since there are seven jets which have to be considered per event, it is expected that the transverse momentum p_T of the seventh jet is quite small. In fact the cuts reject 47% of the signal events. The pre-selection ensures that the detector has the chance to measure all jets and to reduce the background caused by Susy events with other cascades. The left plot of Fig. 5.2 shows that these background events are more dominant in the region that is rejected by the p_T cut. However, many signal events are rejected as well: Out of the 356 matched events, there are 189 left after these cuts.

Figure 5.3 shows the matching control plots after this pre-selection. Both ΔE, and ΔR meet the expectations.

5.2 The "Truth" Scenario

Here a very clear and controlled scenario is discussed. This "truth" scenario is characterized by the following:

- All events have the cascade that is searched for.
- All jets can be matched to a Monte Carlo truth parton.
- All jets are assigned to the correct position in the cascade.
- The pre-selection is applied.

5.2.1 Initial Values

The iterative approach of the kinematic fit needs initial values to start with. The initial values of the 4-momenta of the jets are the measured jet momenta.

For the LSPs there are no measurements and their initial values have to be chosen carefully. For an arbitrary choice of momenta the fit might not find the global minimum or might not converge at all. Since the mass difference of the χ_2^0 / $\chi_1^\pm$ and their daughters are small compared to the released energy in the squark decay, both the LSP and the Z^0 / $W^\pm$ are boosted in the same direction. Following this argument, the direction of the LSP is chosen as the direction of the Z^0 / $W^\pm$.

It seems necessary to fulfill the mass constraint on the χ_2^0 / $\chi_1^\pm$ mass in the first step to reduce the tension on the LSP in the first iteration. This can be achieved by the choice of the magnitude of the LSP momentum. The mass constraint of the χ_2^0 / $\chi_1^\pm$ is

$$f(x) = M^2_{\chi_2^0/\chi_1^\pm} - \left(P_{Z/W} + P_{LSP}\right)^2 = 0. \tag{5.1}$$

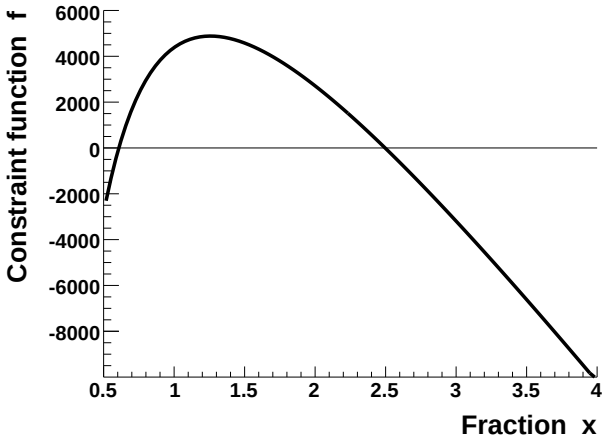

Figure 5.4: Typical plot of the constraint function 5.2 w.r.t. x for one event. In this case there are two real solutions. In other cases the curve doesn't hit the $f = 0$ axis and there is no real solution.

With the fraction of the magnitude of the 3-momenta $x = |p_{LSP}|/|p_{Z/W}|$ this can be written as

$$f(x) = M^2_{\chi_2^0/\chi_1^\pm} - \left(E_{Z/W} + \sqrt{M^2_{LSP} + x^2 \boldsymbol{p}^2_{Z/W}}\right)^2 + (1+x)^2 \boldsymbol{p}^2_{Z/W} = 0 \tag{5.2}$$

Figure 5.4 shows a typical dependence of this function w.r.t. x in the real plane. There are two real solutions one with $|p_{LSP}| < |p_{Z/W}|$ and one with $|p_{LSP}| > |p_{Z/W}|$.

The Newton method is used to determine x. The solution with $x < 1$ leads to better results of the fitter in this Susy scenario. With the other solution the fit converges systematically at too high energies of the LSPs.

But in many events this curve lies completely below the $f = 0$ axis and there is no real solution at all. Due to fluctuations and mismeasurements of the jets, the energy of the Z^0 / $W^\pm$ can be too large. Since the released energy in this decay is small such mismeasurements have the effect that the decay is no longer allowed: The summed mass of the daughter particles (LSP and $Z^0/W^\pm$) is larger than the mass of the mother particle ($\chi_2^0/\chi_1^\pm$). In this case the maximum of the curve is taken.

5.2.2 χ^2 and χ^2 Probability

Figure 5.5 shows the χ^2 distribution and the χ^2 probability of the "truth" scenario fit. The true masses of the Susy particles and the mean mass of the Z^0 and $W^\pm$ has been used as mass constraints. The transverse momentum constraint forces the summed x

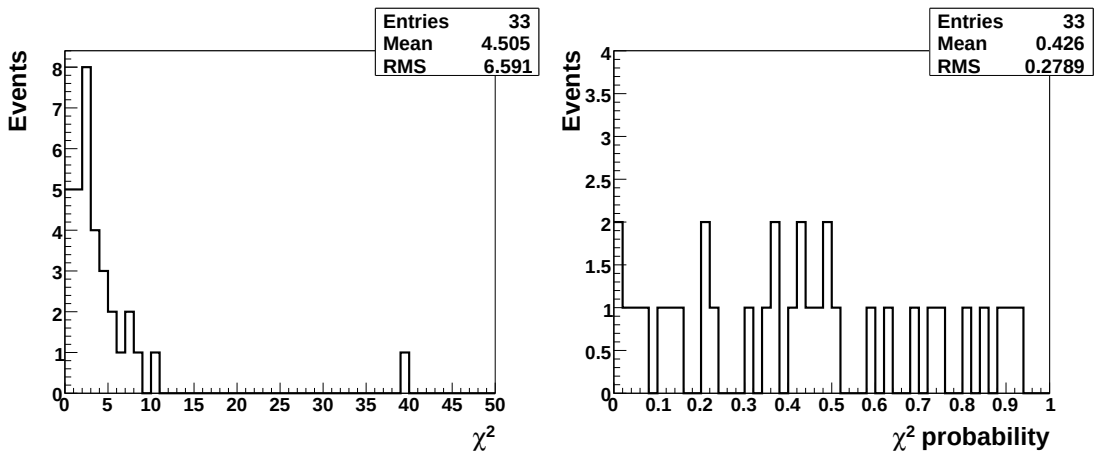

Figure 5.5: Left: The χ^2 distribution after fitting 202 events with the true masses of the supersymmetric particles as constraints. Right: The corresponding probability for three degrees of freedom is flat as expected.

and the y components of all jets (including the ISR jet) and the LSPs to zero. The LSP momenta enter the fit as unmeasured parameters with initial values as described above.

The χ^2 distribution agrees with the three degrees of freedom of the problem (6 unknowns, 9 constraints). Therefore the χ^2 probability is evenly distributed over the whole range from 0 to 1. The problem of this result is obvious as well: Only 35 of the 202 signal events converge at all. The reason is either that no minimum in the χ^2 potential is found (ΔS doesn't get smaller than 0.1 within the allowed 20 iterations) or the constraints are not fulfilled sufficiently ($F > 0.1$). For most of the not converging events the latter one is the case. The situation doesn't change significantly if the number of allowed iterations is increased. The procedure mostly finds a minimum (ΔS is small) but this minimum is not the one that is searched for since the constraints are not fulfilled.

Take LSPs as Measured Particles

To achieve the convergence of more events the LSPs are dealt as measured particles. This prevents the fitting procedure from changing the LSP momenta much from the initial values which are not too far away from the true values as described in section 5.2.1.

This makes a careful error estimation necessary. If the error that is set on the LSP momenta is too large the problems that occur with a parametrization as unmeasured particles would stay. "Unmeasured" in this context is equivalent to an infinite error. If the error is chosen too small the true LSP momentum might be suppressed.

The argumentation for the error estimation is quite similar to the choice of the initial values of the LSPs in section 5.2.1:

In the rest frame of the mother particle χ_2^0 / $\chi_1^\pm$ the momenta of the LSP and the Z^0 / $W^\pm$ have to be negatively equal and relatively small due to the small mass difference.

This can be easily transfered into the rest frame of the Z^0 / $W^\pm$ that is known by the measurement of the decay products. In this rest frame (marked with $\star$) energy and momentum conservation requires

$$\boldsymbol{P}^\star_{Z/W} = \boldsymbol{P}^\star_\chi - \boldsymbol{P}^\star_{\mathrm{LSP}} \tag{5.3}$$

$$\begin{pmatrix} M_{Z/W} \\ 0 \\ 0 \\ 0 \end{pmatrix} = \begin{pmatrix} E^\star_\chi = \sqrt{M^2_\chi + \boldsymbol{p}^{\star 2}} \\ \\ \boldsymbol{p}^\star \\ \\ \end{pmatrix} - \begin{pmatrix} E^\star_{\mathrm{LSP}} = \sqrt{M^2_{\mathrm{LSP}} + \boldsymbol{p}^{\star 2}} \\ \\ \boldsymbol{p}^\star \\ \\ \end{pmatrix} \tag{5.4}$$

with the spatial momentum denoted as $\boldsymbol{p}^\star$

Since the masses are assumed to be known, the magnitude of the momentum $\boldsymbol{p}^\star$ can be calculated.

This leads to a first approximation of the LSP momenta. Since only the magnitude and not the direction is known, the LSP momentum can be limited in the Z^0 / $W^\pm$ rest frame to the surface of a sphere with radius $\boldsymbol{p}^\star$.

This surface has been used as a parametrization of the LSP. Although the argumentation is true in principle, it has not succeeded in practice: Mismeasurements and uncertainties in p_T balance deranges the whole kinematic system and the best solution for the LSP momentum is not located exactly on the surface and can therefore not be found. The solution which is found by the procedure instead mostly does not fulfill the constraints sufficiently. And therefore the event is referred to as not converged.

Therefore a box with the diameters of this sphere along the x-axis, the y-axis, and the z-axis as edge lengths is used as the range, where the LSP momentum is allowed.

It would be an over-estimation using the whole box as errors on the x, y, and z component of the LSP momentum since the complete area is covered where the momentum is kinematically allowed to lie.

The Monte Carlo information of the LSP momenta has been used to fit the distribution of the true momentum components to a Gaussian. The standard deviation of this Gaussian is used as an error estimation in this rest frame.

Finally the edges of this reduced box are Lorentz boosted in the laboratory system and are used as the error range of the LSPs.

This change in parametrization should change the χ^2 distribution since the LSPs contribute as measured particles. Even if it doesn't make sense from a physical point of view to handle an unmeasurable particle like a measured one, statistically this could be unobjectionable. The condition is that the true LSP momentum agrees with an event dependent Gaussian with the Z^0 / $W^\pm$ momentum as mean and the described error estimation as width.

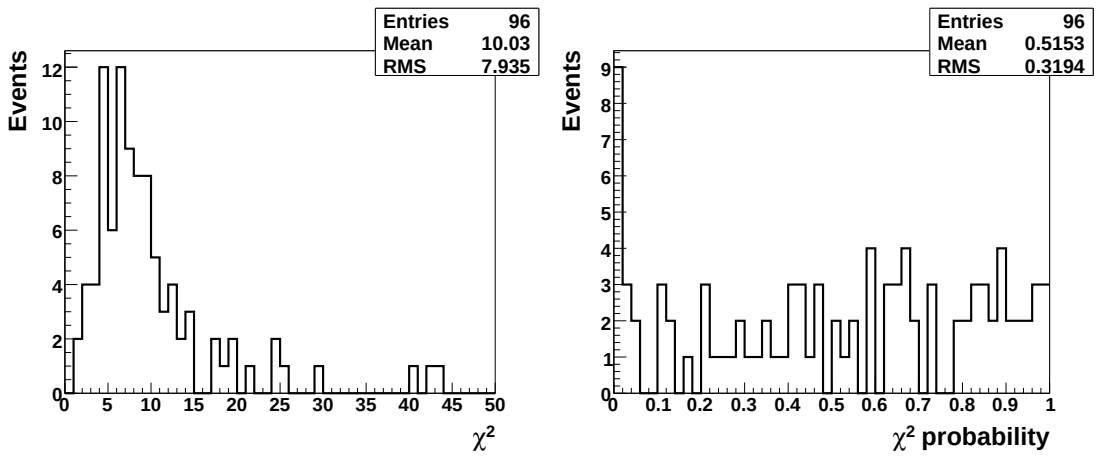

Figure 5.6: Left: The χ^2 distribution if the LSP momenta are parametrized as measured values with an error estimation as described in the text. Right: The corresponding probability for nine degrees of freedom.

The degrees of freedom for the new parametrization become equal to the number of constraints since there are no unmeasured variables in the fit anymore. The χ^2 distribution and the χ^2 probability in Fig. 5.6 are consistent with this new number of degrees of freedom. However, some events accumulate close to a probability of zero. Mismatched jets and the ISR problem could be responsible for this. The number of converged events increases from 33 to 96.

Another test of the method are the momenta of the LSPs. In Fig. 5.7 the values calculated by the fitter are compared with the Monte Carlo truth values. The mean of the energy difference is at zero, there is no systematic shift, and the RMS of the distribution is acceptable. The angular deviation from the Monte Carlo truth information is acceptable as well. The maximum is at the correct position.

The impact of the fit on the measured jets is shown in Fig. 5.8. There is no systematic shift to higher or lower p_T of the jets.

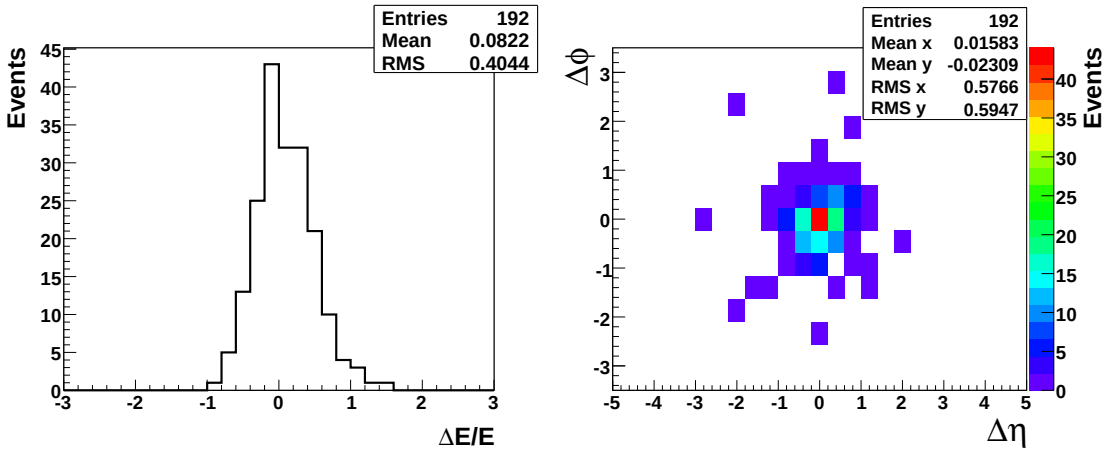

Figure 5.7: Left: The relative energy difference between the LSP calculated by the fitter and the true LSP. Right: The absolute difference in the η-ϕ-plane.

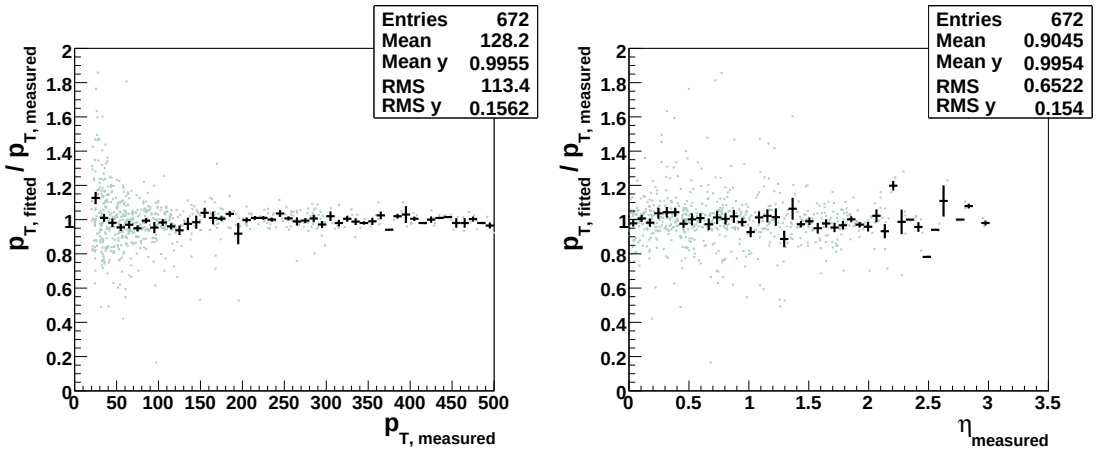

Figure 5.8: The transverse momentum of the seven jets after the fit over the p_T before the fit is plotted versus p_T (left) and versus the pseudorapidity η (right). The green dots are the values per jet, the black crosses mark the mean with errors.

5.2.3 Mass Scans

The method is now going to be tested whether it is suitable to determine the unknown masses of the supersymmetric particles. As the least square fit requires an overconstrained system, it is not possible to loosen up the mass constraints in the fit. Instead, one can perform the fit for different mass hypotheses and compare the resulting χ^2.

This is realized by mass scans. Figures 5.9 to 5.12 show the results of scans of one mass. For each plot the mass of one Susy particle is scanned, the other four Susy masses are set to their true values. In the left plots the best mass hypothesis for every event is histogrammed. In the right plots the χ^2 for this best hypothesis is plotted. The figures show for all masses a clear maximum near the true mass in the histogram. The χ^2 plots differ between the masses. The scan of the squark mass (Fig. 5.10) produces a sharp minimum at the true squark mass. The right plot in Fig. 5.9 has a minimum in the region of the true mass as well, but it is wider and the χ^2 for much higher mass hypotheses are small, too. The χ_2^0 / $\chi_1^\pm$ and the χ_1^0 scans show an increase of the χ^2 towards one side, towards the other side there are no entries at all. If the hypothesis for the $\chi_1^\pm$ / χ_1^0 mass is smaller then the LSP mass hypothesis plus the $W^\pm$ / Z^0 mass there is no solution at all. Since the $\chi_1^\pm$ / χ_1^0 mass is constrained to the invariant mass of the LSP plus the $W^\pm$ / Z^0 4-momentum it has to be at least the sum of those masses.

The next step will be to vary two masses simultaneously. The other two supersymmetric particles are fixed at their true masses. Figures 5.13 to 5.18 show the results. The left plots show the mass hypothesis with the smallest χ^2 . The color shows the χ^2 while the numbers give the number of events which have the smallest χ^2 at the corresponding mass bin. For the right plots all χ^2 are used, not only the best χ^2 per event. For each mass hypothesis the fit has been performed for all events. The resulting χ^2 has been averaged and plotted as color in the figures.

The correlation between two of the masses differ from one mass pair to the next. Figures 5.13 and 5.18 show a linear correlation. If the gluino has a higher mass, the squark is forced to a higher mass as well. The same correlation can be found between the mass of the χ_2^0 / $\chi_1^\pm$ and the LSP. The reason is easy to understand: The χ_2^0 / $\chi_1^\pm$ decay into the LSP. If the hypothetic mass of the χ_2^0 / $\chi_1^\pm$ is too high, more released energy has to be captured somewhere else. Therefore, the LSP is forced to have a higher mass.

The other mass pairs seem to be more or less uncorrelated. The cut-off in Figs. 5.14 to 5.17 is caused by the fixed mass of the LSP in Figs. 5.14 and 5.16, and the fixed mass of the χ_2^0 / $\chi_1^\pm$ in Figs. 5.15 and 5.17. The mass of the χ_2^0 / $\chi_1^\pm$ has to be at least $M(\chi_1^0) + M(Z^0/W^\pm)$.

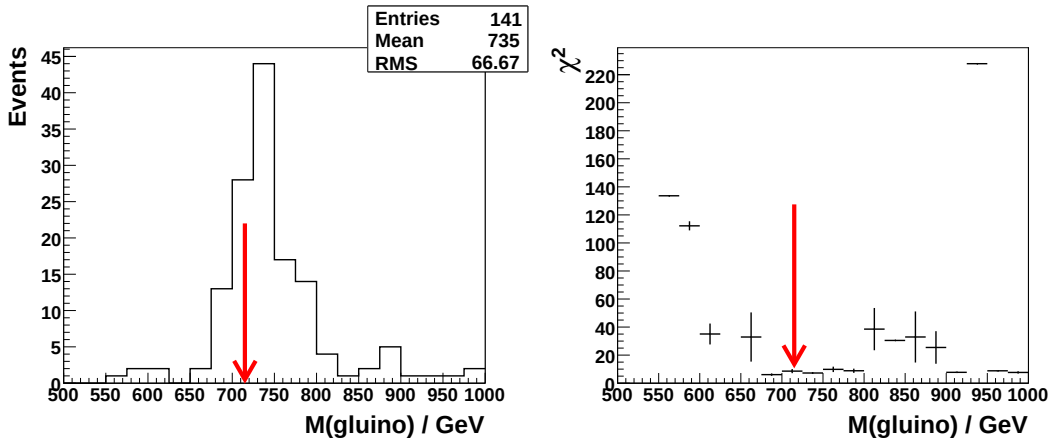

Figure 5.9: Scanning the gluino mass. The other masses are fixed to their true values. Left: The mass hypothesis with the smallest χ^2 per event is histogrammed. The true mass (red arrow) is 715 GeV. Right: The smallest χ^2 per event.

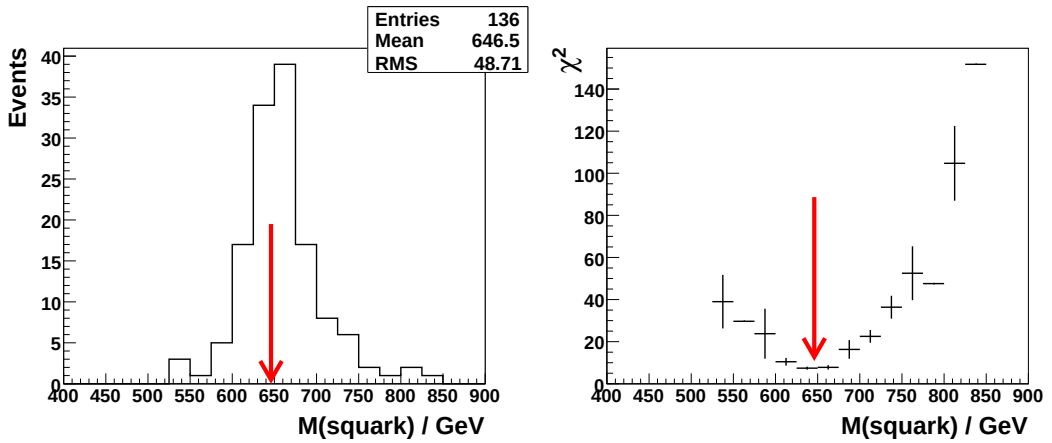

Figure 5.10: Scanning the squark mass. Left: The mass hypothesis with the smallest χ^2 per event is histogrammed. The mean value of the true masses is 646 GeV. Right: The smallest χ^2 per event.

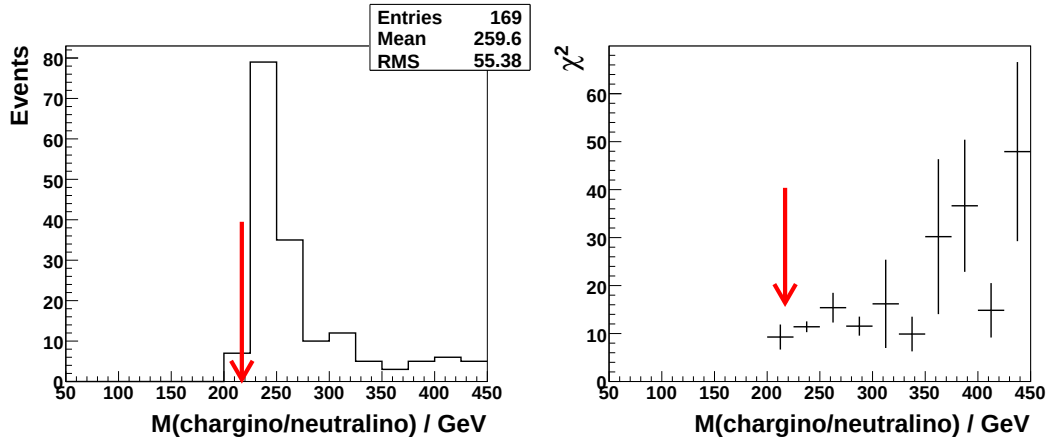

Figure 5.11: Scanning the χ_2^0 / $\chi_1^\pm$ mass. Left: The mass hypothesis with the smallest χ^2 per event is histogrammed. The true mass is 217 GeV. Right: The smallest χ^2 per event.

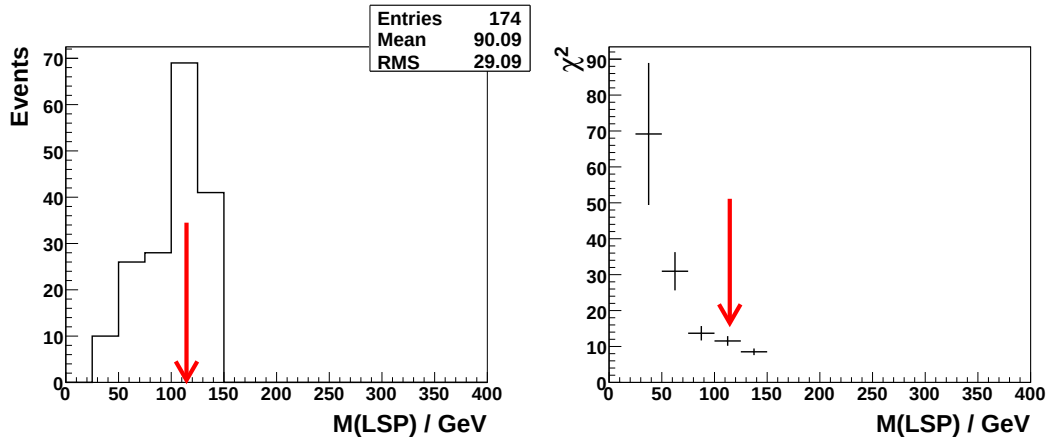

Figure 5.12: Scanning the χ_1^0 mass. Left: The mass hypothesis with the smallest χ^2 per event is histogrammed. The true mass is 114.5 GeV. Right: The smallest χ^2 per event.

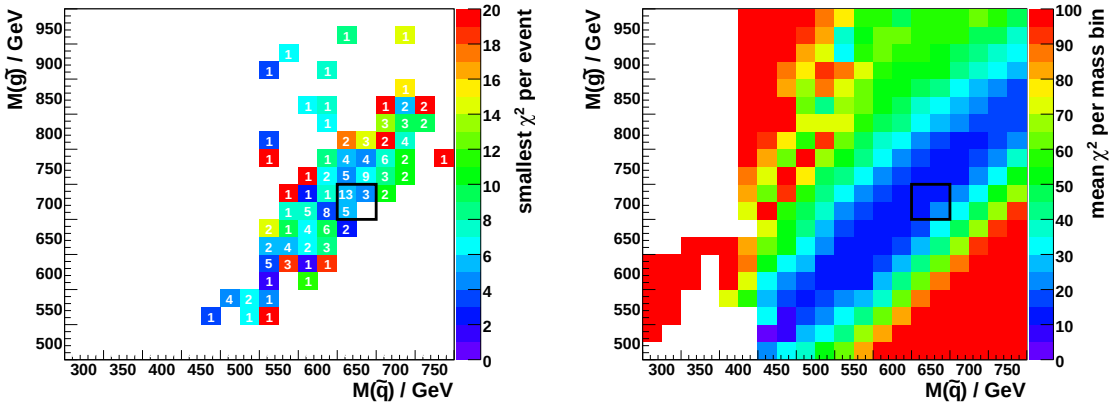

Figure 5.13: Simultaneous scanning of squark and gluino mass. Left: the best hypothesis per event, right: the average of all events per hypothesis.

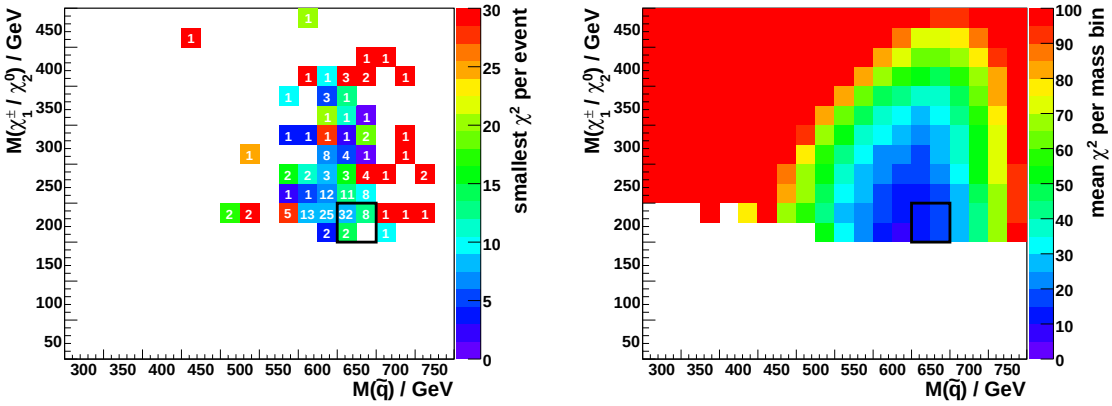

Figure 5.14: Simultaneous scanning of squark and χ_2^0 / $\chi_1^\pm$ mass.

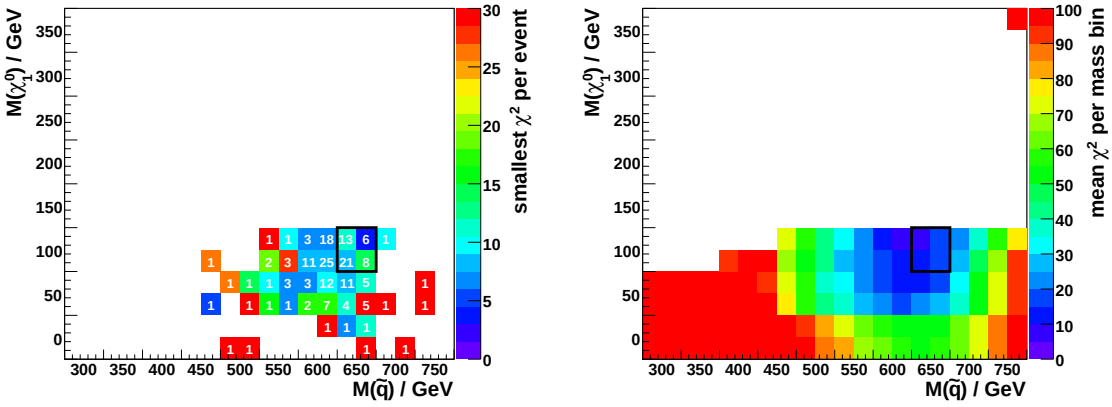

Figure 5.15: Simultaneous scanning of squark and LSP mass.

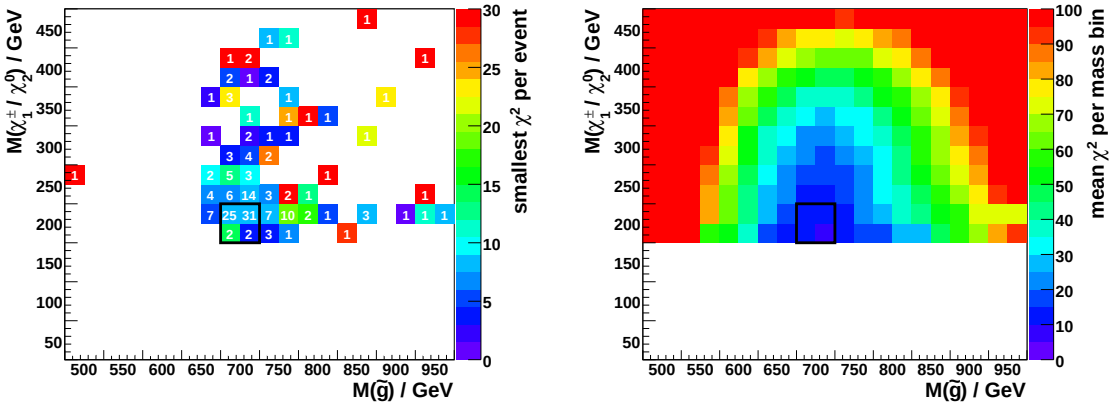

Figure 5.16: Simultaneous scanning of gluino and χ_2^0 / $\chi_1^\pm$ mass.

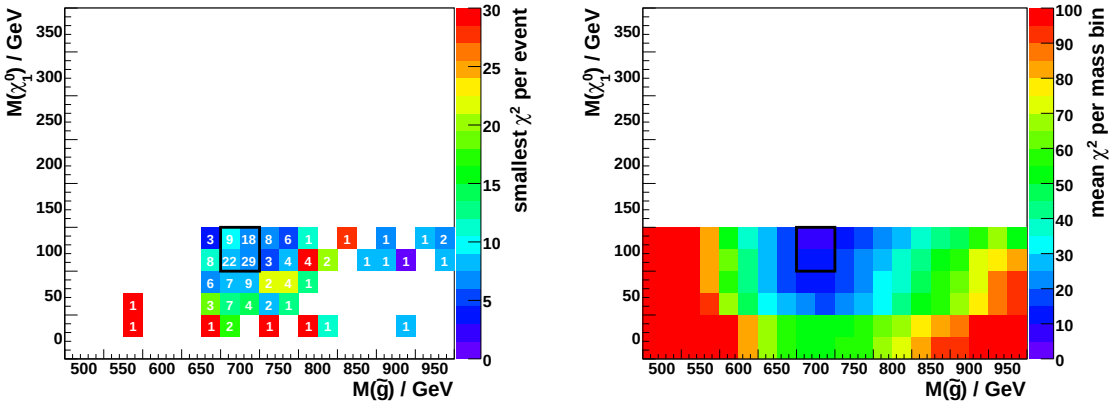

Figure 5.17: Simultaneous scanning of gluino and LSP mass.

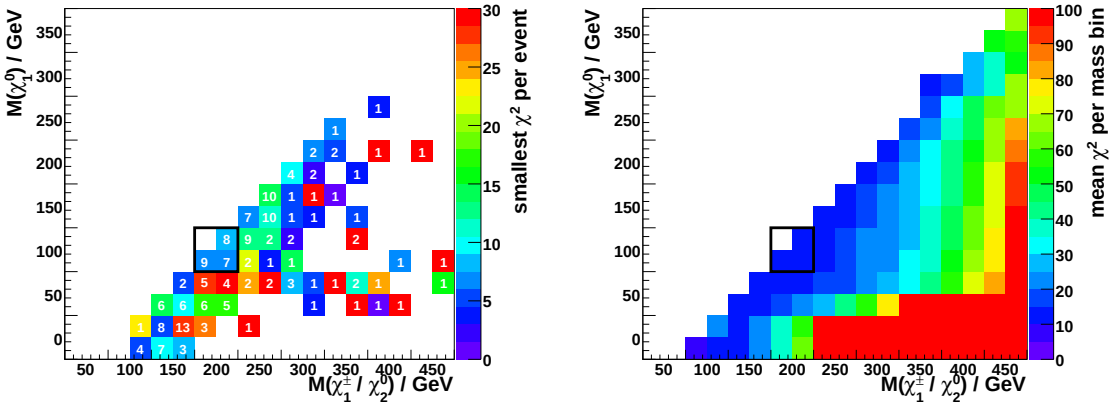

Figure 5.18: Simultaneous scanning of χ_2^0 / $\chi_1^\pm$ and LSP mass.

$M(LSP)$ offset	$M(\chi_2^0/\chi_1^\pm)$ offset							
+150							5.19(a)	5.19(b)
+100						5.19(c)	5.19(d)	
+50					5.19(e)	5.19(f)		
0				5.20(a)	5.20(b)			
−50			5.20(c)	5.20(d)				
−100	5.20(e)	5.20(f)						
	−100	−50	0	+50	+100	+150	+200	

Table 5.1: Scheme of the scanning of all masses. The Figs. 5.19(c) to 5.20(f) show the scanning of the squark and gluino masses for different hypotheses for the χ_2^0 / $\chi_1^\pm$ and LSP masses, denoted as offset to the true masses.

5.2.4 Simultaneous Scanning of All Involved Susy Masses

Till now certain areas in the mass parameter space can be excluded. But since two masses have been fixed at their true values, information from Monte Carlo has been used.

In this section the whole four-dimensional mass parameter space will be scanned. The representation of the results (Figs. 5.19 and 5.20) is done in two-dimensional plots where the squark and the gluino masses are scanned. To include the χ_2^0 / $\chi_1^\pm$ and LSP masses each plot is calculated for another mass hypothesis for these masses.

The grid that is used for the χ_2^0 / $\chi_1^\pm$ and LSP mass hypotheses has the following structure: The two plots in each line have the same hypothesis for the LSP mass, which is given leftmost in each line relatively to the true LSP mass. The hypotheses for the χ_2^0 / $\chi_1^\pm$ mass differ within one line by 50 GeV, which is given below the plots. As shown in Fig. 5.18 the χ_2^0 / $\chi_1^\pm$ and LSP masses are highly correlated. Therefore, the range of the χ_2^0 / $\chi_1^\pm$ mass scanning has to depend on the current mass hypothesis for the LSP mass to get useful results. Since there is a lower bound $M(\chi_2^0/\chi_1^\pm) \geq M(\chi_1^0) + M(Z^0/W^\pm)$ the χ_2^0 / $\chi_1^\pm$ mass scanning in the $M(LSP) = \text{true} + 150\,\text{GeV}$ line starts with $M(\chi_2^0/\chi_1^\pm) = \text{true} + 150\,\text{GeV}$, in the $M(LSP) = \text{true} + 100\,\text{GeV}$ line with $M(\chi_2^0/\chi_1^\pm) = \text{true} + 100\,\text{GeV}$ and so on. So, the left column corresponds to the diagonal in Fig. 5.18. In the right column the χ_2^0 / $\chi_1^\pm$ mass hypothesis is increased by 50 GeV relatively to the diagonal. Table 5.1 shows this structure of the simultaneous scanning of all involved Susy masses.

The colors in the plots show (equal to the right plots in Figs. 5.14 to 5.17) the mean

χ^2 probability per mass bin. The numbers are equivalent to those in the left plots in Figs. 5.14 to 5.17. They count how many events have their smallest χ^2 for the corresponding gluino-squark mass hypothesis.

The averaged χ^2 probability over all events can be interpreted as a measure of the probability for the mass hypothesis. For the true mass hypothesis we expect an uniform distributed χ^2 probability. Therefore, the average should be 0.5. The number of events for which a hypothesis delivers the smallest χ^2 is another possibility to distinguish between good and bad hypotheses.

The first column of the plots shows the best χ^2 probabilities in each line. This confirms the correlation in Fig. 5.18. The mean χ^2 probability gets worse the more the change of the χ_2^0 / $\chi_1^\pm$ mass differs from the change of the LSP mass independent of the gluino and squark masses.

Figure 5.20(a) in the box shows the results for the true χ_2^0 / $\chi_1^\pm$ and LSP mass hypothesis. The little box in the plot shows the mean χ^2 probability for the true hypothesis for all masses. It is near 0.5 as expected. However, other squark-gluino mass hypotheses towards lower masses deliver a mean χ^2 probability of the same size. But the true hypothesis is supported by the number, that indicates that among all tested squark and gluino mass hypotheses most events have the smallest χ^2 for the true one.

Going the χ_2^0 / $\chi_1^\pm$-LSP diagonal downwards (Fig. 5.20(c)) we find some bins with good mean χ^2 probabilities for lighter squark-gluino masses which can't be excluded by the number either.

Figure 5.20(e) ($M(\chi_2^0/\chi_1^\pm) = \text{true} - 100\,\text{GeV}$, $M(LSP) = \text{true} - 100\,\text{GeV}$) is for the lower edge of the LSP mass $M(LSP) = 14.5\,\text{GeV}$. Here only 39 events converge for any squark-gluino hypothesis.

Going the χ_2^0 / $\chi_1^\pm$-LSP diagonal upwards (Fig. 5.19, left plots) the squark and gluino masses are forced to larger values (note the different ranges in gluino and squark scanning) but the probability gets worse. And there is a remarkable difference between the squark-gluino hypothesis with the best probability and those which is the best for most events. The χ^2 probability distributions cannot be flat to explain this behavior. In the bins with a large number this number of events have to have a good probability. If the probability average is nevertheless small, there must be a lot of events with a probability near zero. So these hypotheses can be excluded by the shape of the probability distribution.

These final results of the "truth" scenario are summarized in Figs. 5.21 and 5.22. The averaged χ^2 probabilities that are shown in here don't depend on the hypotheses for the masses of the other Susy particles: Each bin in Fig. 5.21 shows the best probability of all tested squark-gluino masses under a hypothesis for the $\chi_2^0/\chi_1^\pm$ and LSP masses. And conversely, in Fig. 5.22 the best hypotheses for the $\chi_2^0/\chi_1^\pm$ and LSP masses are plotted w. r. t. the squark and the gluino mass.

The correlations seen in Figs. 5.13 and 5.18 are confirmed by the simultaneous scanning of all masses:

$M(LSP) = \text{true} + 150\,\text{GeV}$

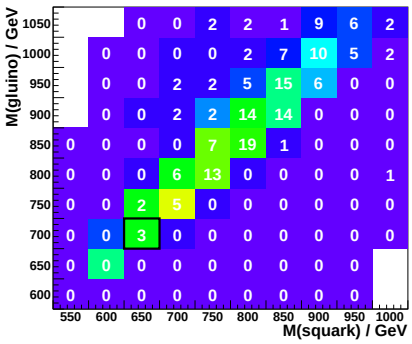

(a) $M(\chi_2^0/\chi_1^\pm) = \text{true} + 150\,\text{GeV}$

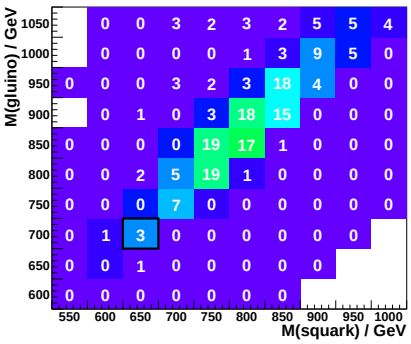

(b) $M(\chi_2^0/\chi_1^\pm) = \text{true} + 200\,\text{GeV}$

$M(LSP) = \text{true} + 100\,\text{GeV}$

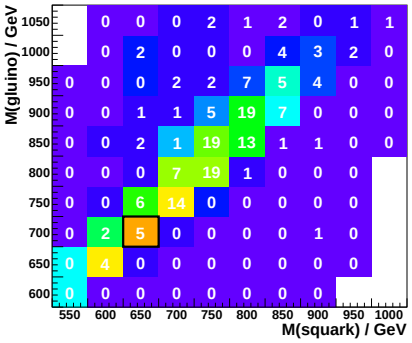

(c) $M(\chi_2^0/\chi_1^\pm) = \text{true} + 100\,\text{GeV}$

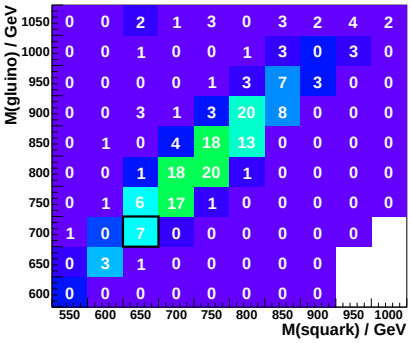

(d) $M(\chi_2^0/\chi_1^\pm) = \text{true} + 150\,\text{GeV}$

$M(LSP) = \text{true} + 50\,\text{GeV}$

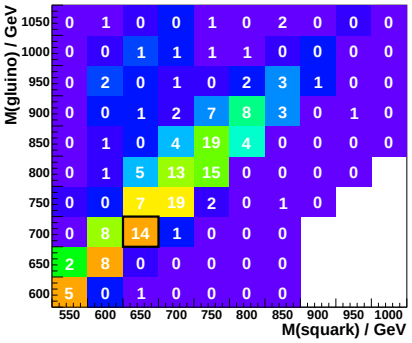

(e) $M(\chi_2^0/\chi_1^\pm) = \text{true} + 50\,\text{GeV}$

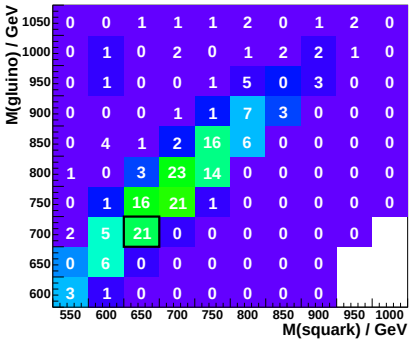

(f) $M(\chi_2^0/\chi_1^\pm) = \text{true} + 100\,\text{GeV}$

Figure 5.19: Scanning of all masses in the "truth" scenario part 1

$M(LSP) = \text{true}$

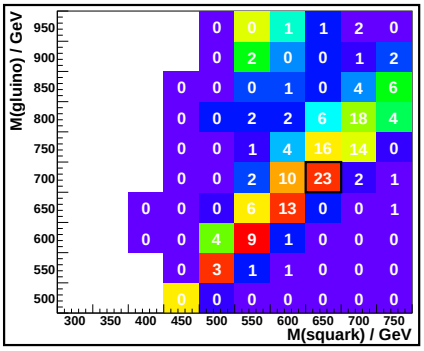

(a) $M(\chi_2^0/\chi_1^\pm) = \text{true}$

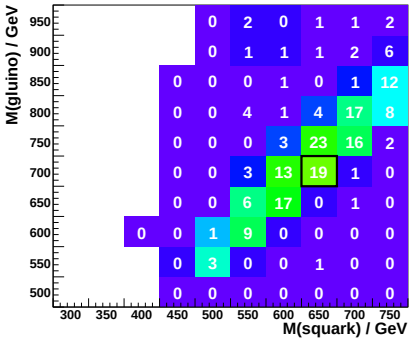

(b) $M(\chi_2^0/\chi_1^\pm) = \text{true} + 50\,\text{GeV}$

$M(LSP) = \text{true} - 50\,\text{GeV}$

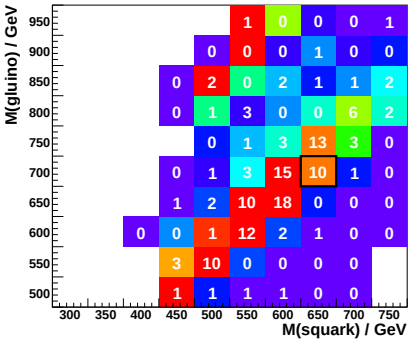

(c) $M(\chi_2^0/\chi_1^\pm) = \text{true} - 50\,\text{GeV}$

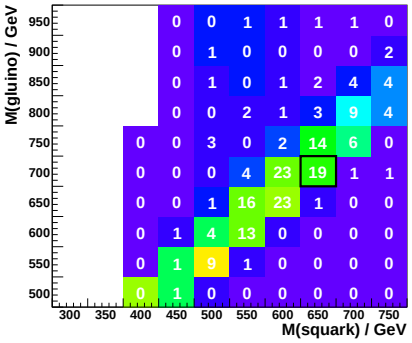

(d) $M(\chi_2^0/\chi_1^\pm) = \text{true}$

$M(LSP) = \text{true} - 100\,\text{GeV}$

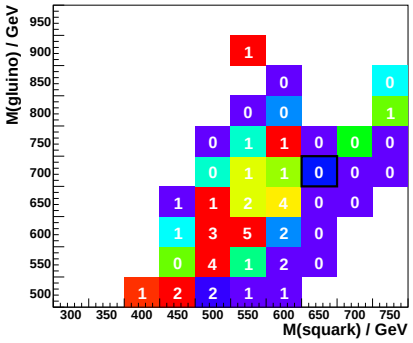

(e) $M(\chi_2^0/\chi_1^\pm) = \text{true} - 100\,\text{GeV}$

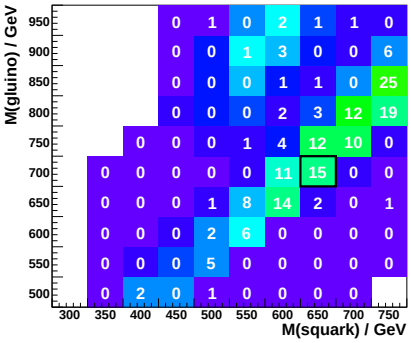

(f) $M(\chi_2^0/\chi_1^\pm) = \text{true} - 50\,\text{GeV}$

Figure 5.20: Scanning of all masses in the "truth" scenario part 2

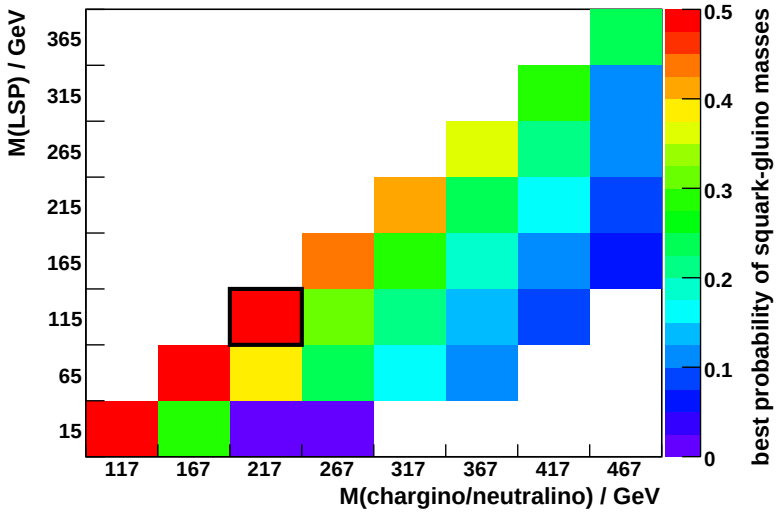

Figure 5.21: The probability for the best squark-gluino mass hypothesis is plotted w. r. t. the masses of the $\chi_2^0/\chi_1^\pm$ and the LSP. The red line marks the 95% C. L.

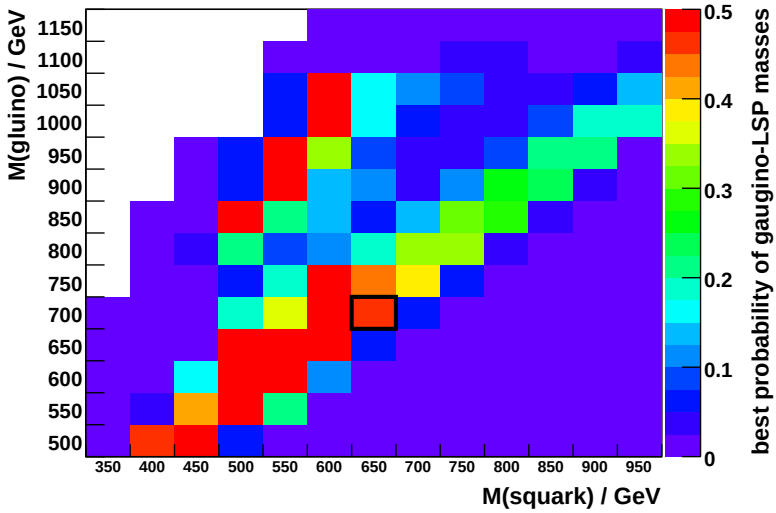

Figure 5.22: The probability for the best $\chi_2^0/\chi_1^\pm$-LSP mass hypothesis is plotted w. r. t. the masses of the squark and gluino. The second area with good hypotheses at higher gluino masses is caused by very few events at low $\chi_2^0/\chi_1^\pm$-LSP hypotheses.

Gluino and Squark:	$M(\tilde{g})$	$\approx$	$M(\tilde{q}) + 50\,\mathrm{GeV}$
Chargino/neutralino and LSP:	$M(\chi_2^0/\chi_1^\pm)$	$\approx$	$M(\chi_1^0) + 100\,\mathrm{GeV}$

However, these results are still generated with Monte Carlo truth information: All jets are matched to the cascade. Hence, the combinatorial problem is not taken into account as well as the problem of selecting all involved jets.

This "truth" scenario is realistic only in the sense that at first the used jet measurements are at detector level, and second that the p_T balance is constructed by these jets and at most one jet from initial state radiation.

5.3 The "Realistic" Scenario

In the scenario discussed before, Monte Carlo truth information has been used. The matching between quarks and reconstructed jets has ensured that no background from wrong combination has to be dealt with and that all jets belonging to the cascade and only these have been taken into account.

5.3.1 Selecting the Jets

In a more realistic scenario this matching of reconstructed jets to the position in the cascade has to be avoided. Instead of the matched jets, the eight hardest jets of the event are taken to perform the kinematic fit. The eighth jet is included to account for possible initial state radiation. In Fig. 5.23 the efficiency of this procedure is illustrated. In about 34% (69 events) of the signal events simulated with Pythia the jets belonging to the cascade are the seven hardest jets measured by the detector. In another 29% (58 events) the softest cascade jet is the eighth hardest jet and taken into the fitting routine as well. The remaining 37% (75 events) enter the fit with at least one jet of the cascade missing.

5.3.2 $Z^0/W^\pm$ Preselection

A difficulty of the "realistic" scenario is the combinatorial problem. If one doesn't know the origin of the jets on the cascade level each combination is possible. With eight jets there are 10 080 possibilities of combination. Trying all these out would cost a lot of computing time. To reduce the number of combinations a pre-selection searching for suitable Z^0 / $W^\pm$ candidates among all dijet combinations is performed. The required dijet mass range is 60 GeV to 125 GeV. The test of this setting is shown in Fig. 5.24. There is quite a large number of true Z^0 / $W^\pm$ lying outside these limits. But most of the events with such a Z^0 / $W^\pm$ don't converge anyway.

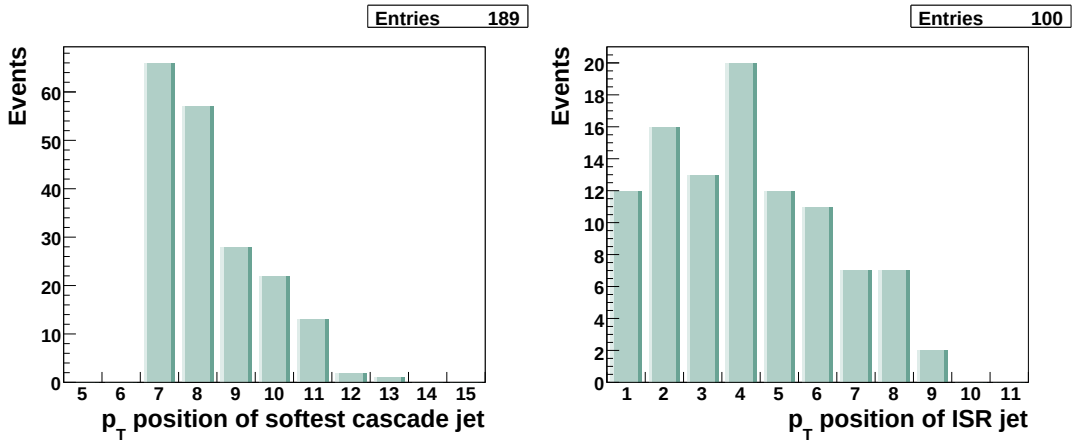

Figure 5.23: Left: Position of the softest jet of the cascade within p_T sorted jets. If an event has an entry at position 7 the seven hardest jets are the seven cascade jets. All events with the softest cascade jets at position 9 or higher loose this jet by the selection since one ISR jet is allowed. Right: Position of the ISR jet within the eight p_T sorted jets. For over half the events an initial state radiation jet can be matched to an ISR parton. This jet is very often harder then some cascade jets.

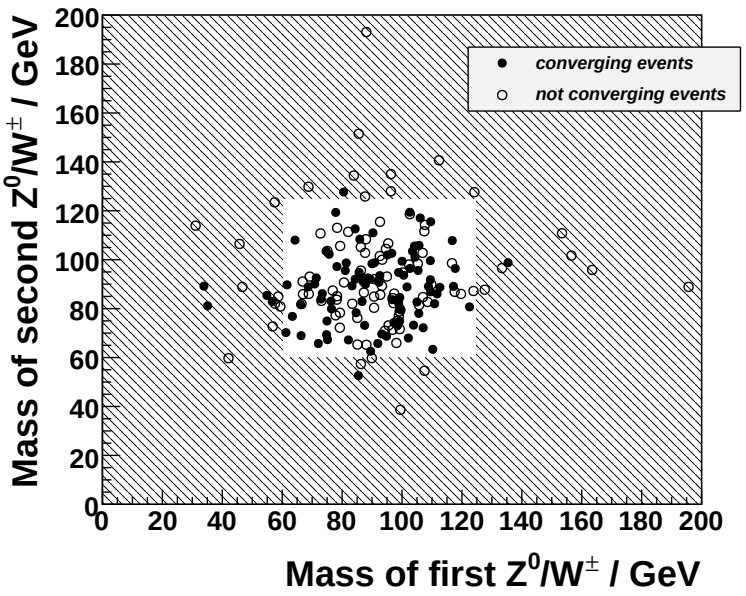

Figure 5.24: Dijet mass of the true Z^0 / $W^{\pm}$ before the fit. All events lying in the hatched area are rejected. The filled dots belong to events that converged in the fit.

This reduces the number of combinatorial hypotheses that have to be tested to an average of about 550 per event.

5.3.3 χ^2 Selection of Combinatorial Hypotheses

At first the "truth" scenario is analyzed as a reference and in order to understand the combinatorial problem. In Fig. 5.25 the distribution of the minimal χ^2 and the χ^2 position of the correct combination is shown. The correct jet combination has the minimal χ^2 in only 16% of the events. For almost 70% a wrong combination produces a better χ^2. The remaining events don't converge for any combination.

The combinatorial problem is reduced strongly: The ratio of the true to all combinatorial hypotheses changes from one over 1260 (or in half of the events even one over 10,080 because of initial state radiation) in the beginning to one over 550 through searching for Z^0 / $W^\pm$ candidates to 16% when only the best hypothesis is accepted.

The wrong combinations that fitted better than the true combination have to be analyzed. A typical error is the change of jets from one branch to the equivalent position in the other branch. This leads often to a combination where some of the decaying particles are associated to jets which construct the same particle in the other branch. In 65 of the events with a wrong combination at least one Z^0 / $W^\pm$ is constructed of jets which belong to one of the Z^0 / $W^\pm$ in the true combination. In 48 of these events this applies to the corresponding squarks as well. Still, in 33 events both Z^0 / $W^\pm$ are constructed of true Z^0 / $W^\pm$ jets and in 15 events both squarks are constructed of true squark jets. In these last-mentioned 15 events the complete branches are switched except of the jet from the gluino decay which is rather soft due to the small mass difference between squark and gluino.

One could expect that the true combination is at least the second or third best, even though it's not the best one. Figure 5.26 shows that this is not correct for many of these events. There is a tail up to quite large numbers of combinations that produce a better χ^2.

5.3.4 Fitting with Full Combinatorics

In Fig. 5.32 the fitting procedure is again done with the signal events, but in a more realistic way: Instead of taking the matched jets the eight hardest jets are used as mentioned on page 57. The plots don't differ much from Fig. 5.25.

The same two dimensional mass scans as before are now reproduced for each mass pair with the signal events but with the eight hardest jets instead of the matched ones and with the whole combinatorial background. The two other Susy masses are fixed at their true values. The plots are shown in Fig. 5.27. For each event and each mass hypothesis the jet combination with the best χ^2 is shown in the plot. The χ^2 probabilities of these combinations are averaged over all events and displayed as color in the figures. The

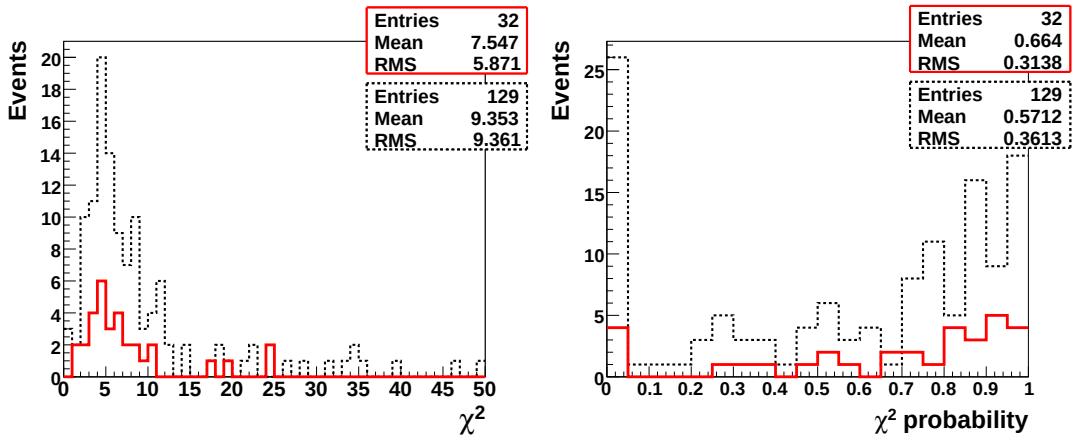

Figure 5.25: Left: Distribution of minimal χ^2 for true and wrong jet combinations. The red line shows the events for which the best combination is the correct one, the black, dashed line shows events for which a wrong jet combination has a better χ^2 . Right: The corresponding χ^2 probability.

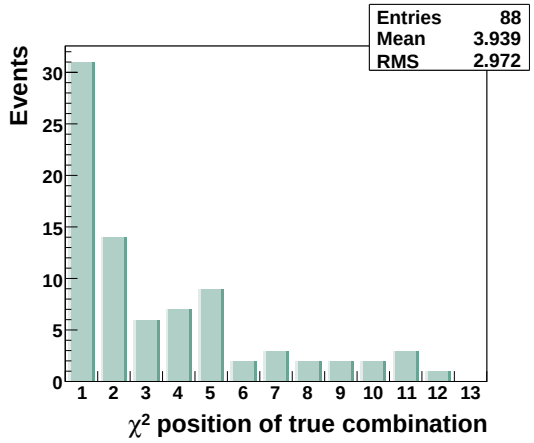

Figure 5.26: The position of the correct combination within a χ^2 sorted list of all combinations which converge in the fit. (The missing 11 events compared with Fig. 5.6 are rejected by the Z^0 / $W^{\pm}$ candidate cut.)

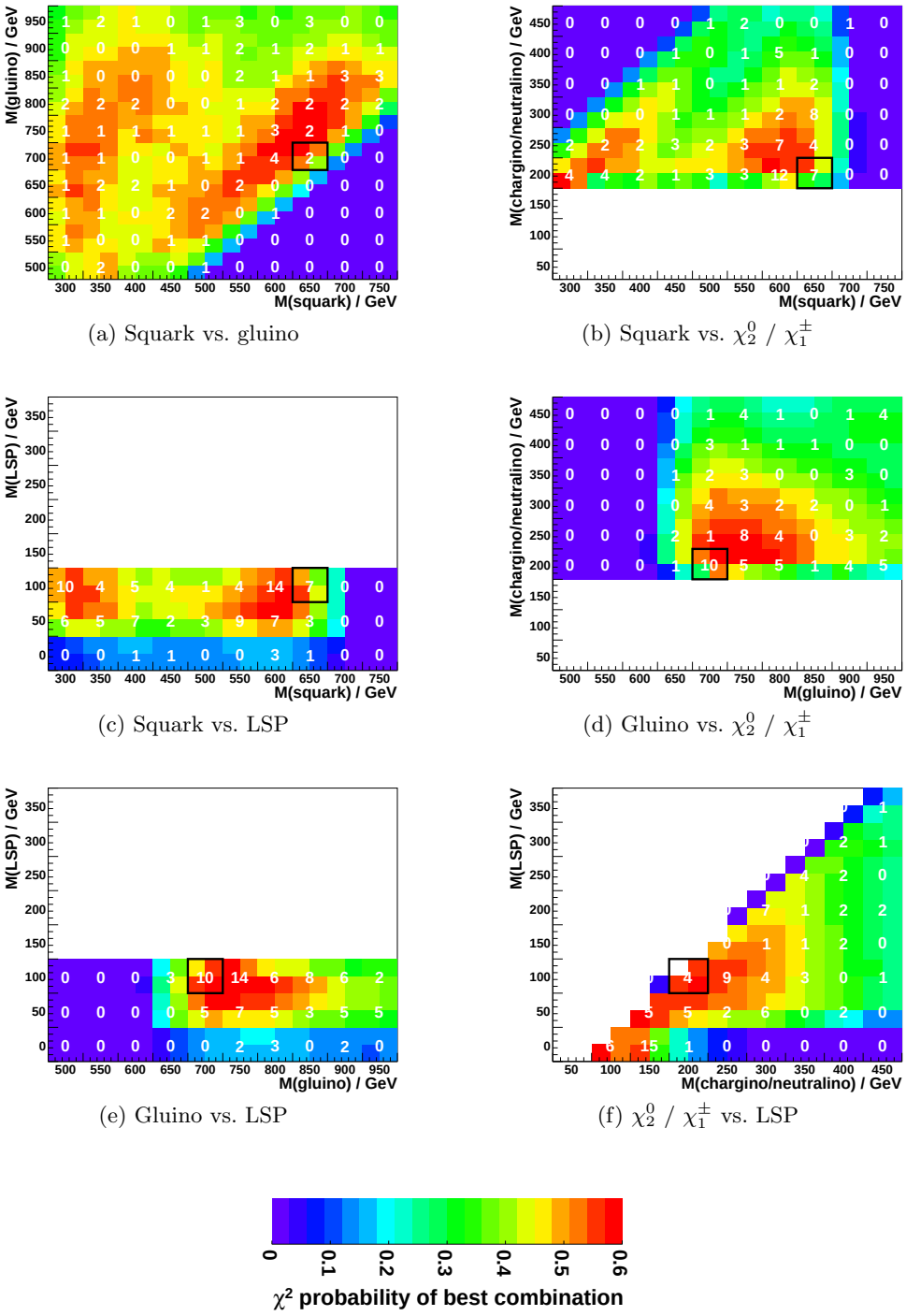

(a) Squark vs. gluino

(b) Squark vs. χ_2^0 / $\chi_1^\pm$

(c) Squark vs. LSP

(d) Gluino vs. χ_2^0 / $\chi_1^\pm$

(e) Gluino vs. LSP

(f) χ_2^0 / $\chi_1^\pm$ vs. LSP

Figure 5.27: Simultaneous scanning of two masses as denoted in the subcaptions. The true masses are marked by a box.

overall best hypothesis per event is counted by the number in the corresponding mass bin. Since these scans are performed with only 100 events the size of the bins containing the numbers is enlarged.

As expected the results in Fig. 5.27 are much worse than the results of the "truth" scenario in Figs. 5.13 to 5.18.

In the three plots where the squark mass is scanned (upper two and middle left) a maximum in the region of the true squark mass appears (which is again marked by a box), but there is another region with good probabilities at much smaller masses of about 300 GeV to 400 GeV. This is almost independent of the masses of the other supersymmetric particles. One possibility is that the hard jet from the squark decay is replaced by a jet with much less energy.

For the other masses the maximum of the χ^2 probability is close to the true masses.

5.3.5 Simultaneous Scanning of All Involved Susy Masses

In Figs. 5.28 and 5.29 the results for the simultaneous scanning of all involved Susy masses are presented the same way as in the "truth" scenario. From the shown hypotheses for the $\chi_2^0/\chi_1^\pm$ and LSP masses only a few can be excluded: The $M(\chi_2^0/\chi_1^\pm) = \text{true} + 150\,\text{GeV}$, $M(LSP) = \text{true} + 150\,\text{GeV}$ plot (Fig. 5.28(a)) and the $M(\chi_2^0/\chi_1^\pm) = \text{true} - 50\,\text{GeV}$, $M(LSP) = \text{true} - 100\,\text{GeV}$ plot (Fig. 5.29(f) have no entries with χ^2 probability average of more than 0.5

For the small $\chi_2^0/\chi_1^\pm$-LSP mass hypotheses the range of good squark-gluino hypotheses becomes wide and towards low masses it is only limited by the range of tested hypotheses. Towards higher $\chi_2^0/\chi_1^\pm$-LSP mass hypotheses the region of good squark-gluino hypotheses gets narrow and to higher masses as seen in the "truth" scenario.

The final result of this section is again one plot where the best χ^2 probability of all tested hypotheses for the squark and the gluino masses is plotted w. r. t. the $\chi_2^0/\chi_1^\pm$ and the LSP mass. It is shown in Fig. 5.30.

The regions with good probabilities within the "realistic" scenario are larger as expected. The correlations between the masses which are found in the "truth" scenario are blurred but still there.

There is no lower bound on the LSP anymore. As shown in Fig. 5.27(f) as well as in Fig. 5.29(e) hypotheses with LSP masses close to zero have good probabilities. The lower bound on the $\chi_2^0/\chi_1^\pm$ mass is only given by the mass of the $Z^0/W^\pm$.

Similar is the situation concerning the squark and gluino mass: The masses with the best probability decrease with the $\chi_2^0/\chi_1^\pm$-LSP mass hypothesis. In Fig. 5.29(c) as well as Fig. 5.29(e) there are no confined regions of preferred hypotheses.

The final result of the scanning of all masses using these "realistic" signal events is again given in two plots. Figure 5.30 shows the probability of the $\chi_2^0/\chi_1^\pm$ and LSP masses independently of the squark and gluino mass. Each of the plots in Figs. 5.28 and 5.29 is represented by one bin which shows the best probability of all tested squark-

$M(LSP) = \text{true} + 150\,\text{GeV}$

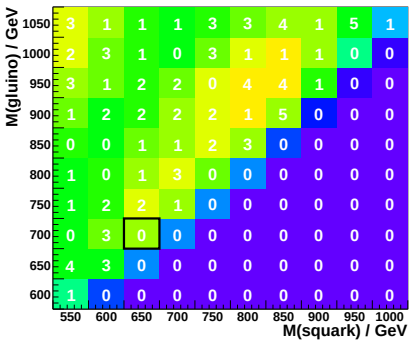

(a) $M(\chi_2^0/\chi_1^\pm) = \text{true} + 150\,\text{GeV}$

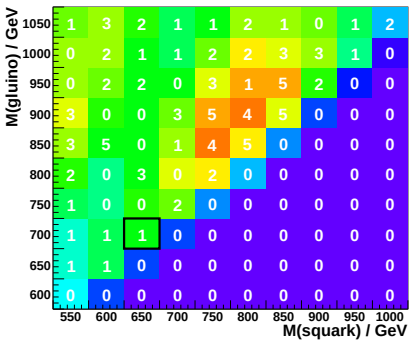

(b) $M(\chi_2^0/\chi_1^\pm) = \text{true} + 200\,\text{GeV}$

$M(LSP) = \text{true} + 100\,\text{GeV}$

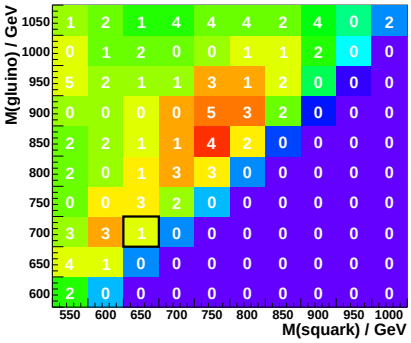

(c) $M(\chi_2^0/\chi_1^\pm) = \text{true} + 100\,\text{GeV}$

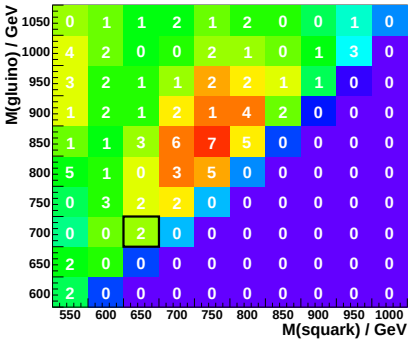

(d) $M(\chi_2^0/\chi_1^\pm) = \text{true} + 150\,\text{GeV}$

$M(LSP) = \text{true} + 50\,\text{GeV}$

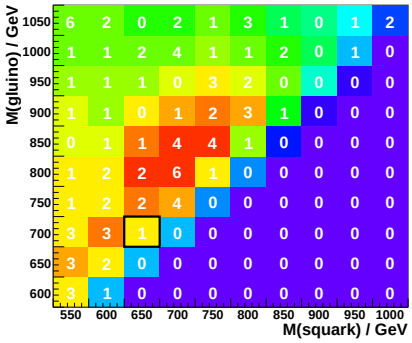

(e) $M(\chi_2^0/\chi_1^\pm) = \text{true} + 50\,\text{GeV}$

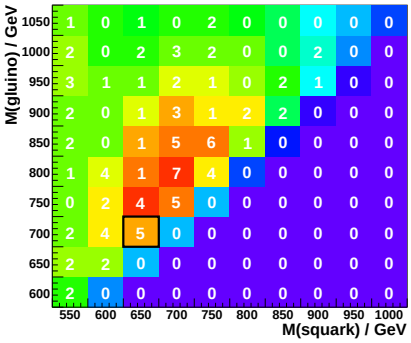

(f) $M(\chi_2^0/\chi_1^\pm) = \text{true} + 100\,\text{GeV}$

Figure 5.28: Scanning of all masses in the "realistic" scenario part 1

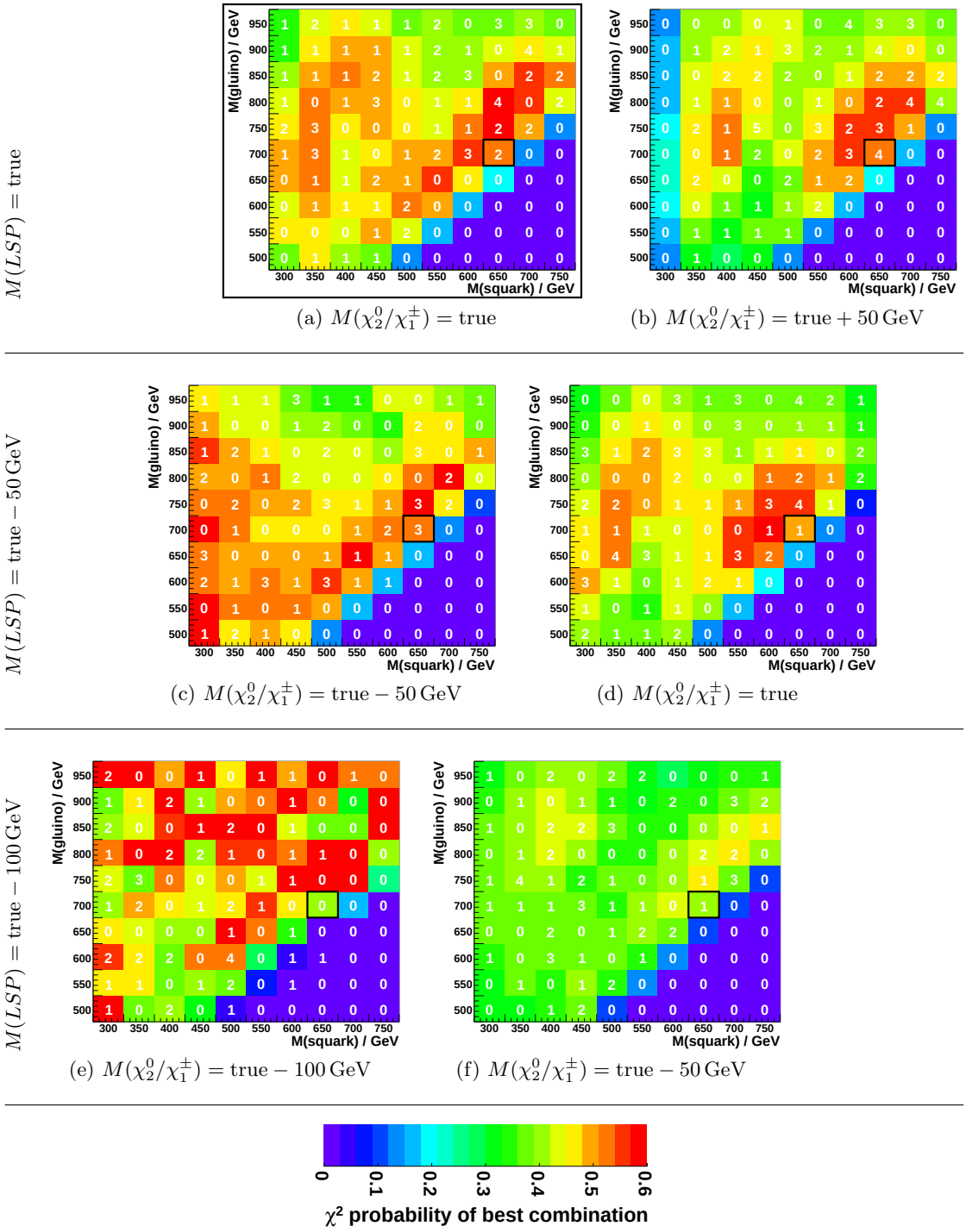

(a) $M(\chi_2^0/\chi_1^\pm) = \text{true}$ (b) $M(\chi_2^0/\chi_1^\pm) = \text{true} + 50\,\text{GeV}$

(c) $M(\chi_2^0/\chi_1^\pm) = \text{true} - 50\,\text{GeV}$ (d) $M(\chi_2^0/\chi_1^\pm) = \text{true}$

(e) $M(\chi_2^0/\chi_1^\pm) = \text{true} - 100\,\text{GeV}$ (f) $M(\chi_2^0/\chi_1^\pm) = \text{true} - 50\,\text{GeV}$

Figure 5.29: Scanning of all masses in the "realistic" scenario part 2

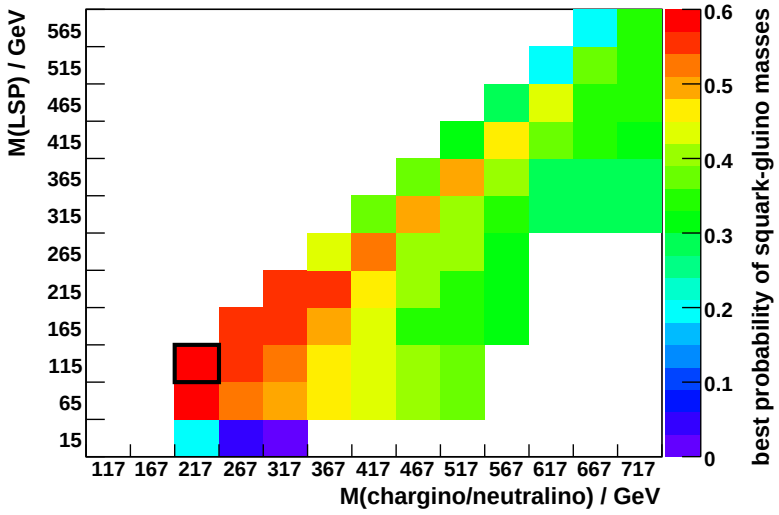

Figure 5.30: The probability for the best squark-gluino mass hypothesis is plotted w. r. t. the masses of the $\chi_2^0/\chi_1^\pm$ and the LSP.

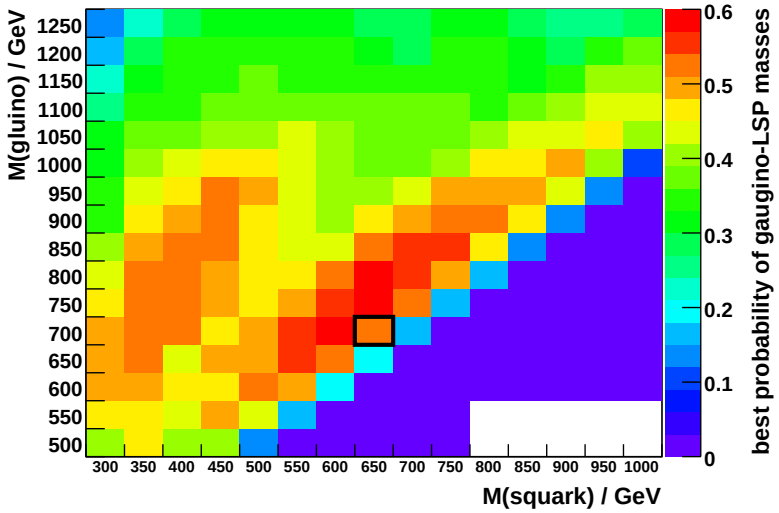

Figure 5.31: The probability for the best $\chi_2^0/\chi_1^\pm$-LSP mass hypothesis is plotted w. r. t. the masses of the squark and gluino. The light $\chi_2^0/\chi_1^\pm$ masses are not taken into account. For these $\chi_2^0/\chi_1^\pm$ mass hypotheses a lot of squark-gluino hypotheses have a good probability as shown in Figs. 5.29(c) and 5.29(e).

gluino masses. Figure 5.31 shows the probability of the squark and the gluino mass independently of the $\chi_2^0/\chi_1^\pm$ and LSP masses. Therefore the best probability of all plots in Figs. 5.28 and 5.29 per mass bin is summarized in one plot. Figures 5.29(c) and 5.29(e) is omitted since there are many good hypotheses with only a few entries.

5.3.6 Susy Background

Since only one special cascade is studied in the analysis, there is the huge background from other supersymmetric events. After applying the pre-selection cuts, the event sample can be divided in three parts:

- 1276 events contain the cascade that is searched for.
- 17,332 events have only one of the two decay branches from the cascade that is searched for.
- 21,412 events do not fit to the cascade at all.

This different backgrounds will now be compared. In the first step the masses of the supersymmetric particles are set to their true values. The combinatorial background has to be taken into account in such a way that for each event the jet combination with the smallest χ^2 after the fit is taken.

Figures 5.33 show the χ^2 distribution and the χ^2 probability of the two kinds of Susy background. In comparison to Fig. 5.32 the χ^2 distribution is shifted towards larger values as expected.

The Susy background will now be studied with mass scans as done before with the signal events. This will test if the method of kinematic fits not only finds the true mass of the involved particles but also rejects the background of other decay cascades. This is expected since other event topologies should not fit to the assumed constraints.

The mass scans of the Susy background events start immediately with the hypotheses scanning of two masses simultaneously. The results are displayed in Fig. 5.34. For better orientation the true masses of the signal events are marked by a black box as in the previous plots. Although these particles occur in the background events as well, it is not surprising that the regions with the best probabilities do not meet these values. The kinematic fit is sensitive to the whole topology of an event not only to single particles.

Nevertheless there are regions with good probabilities. The reason for that might be misinterpretations of invariant masses. If for example a chargino decays according to the signal cascade but due to final state radiation there are four jets plus LSP which construct its mass (instead of three as expected) the kinematic fit would interpret this chargino as a squark. On the other hand, if one weak jet of a squark decay is rejected by the pre-selection the topology of this decay looks like a decaying chargino. In this case the kinematic fit would prefer hypotheses with larger $\chi_2^0/\chi_1^\pm$ masses.

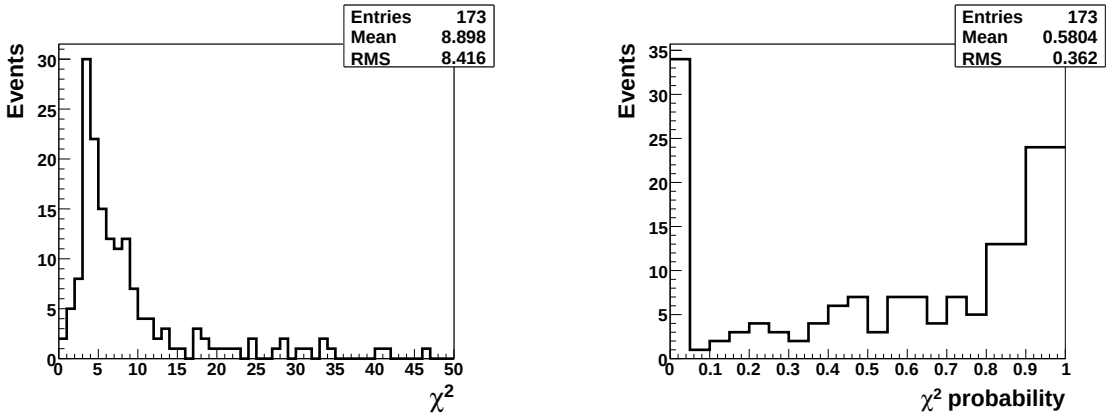

Figure 5.32: Events with the cascade that is searched for and successful matching between partons and jets. In contrast to Fig. 5.25 this matching is ignored here and the eight hardest jets are taken to do the fit. Left: Distribution of minimal χ^2 of combinations. Right: The corresponding χ^2 probability.

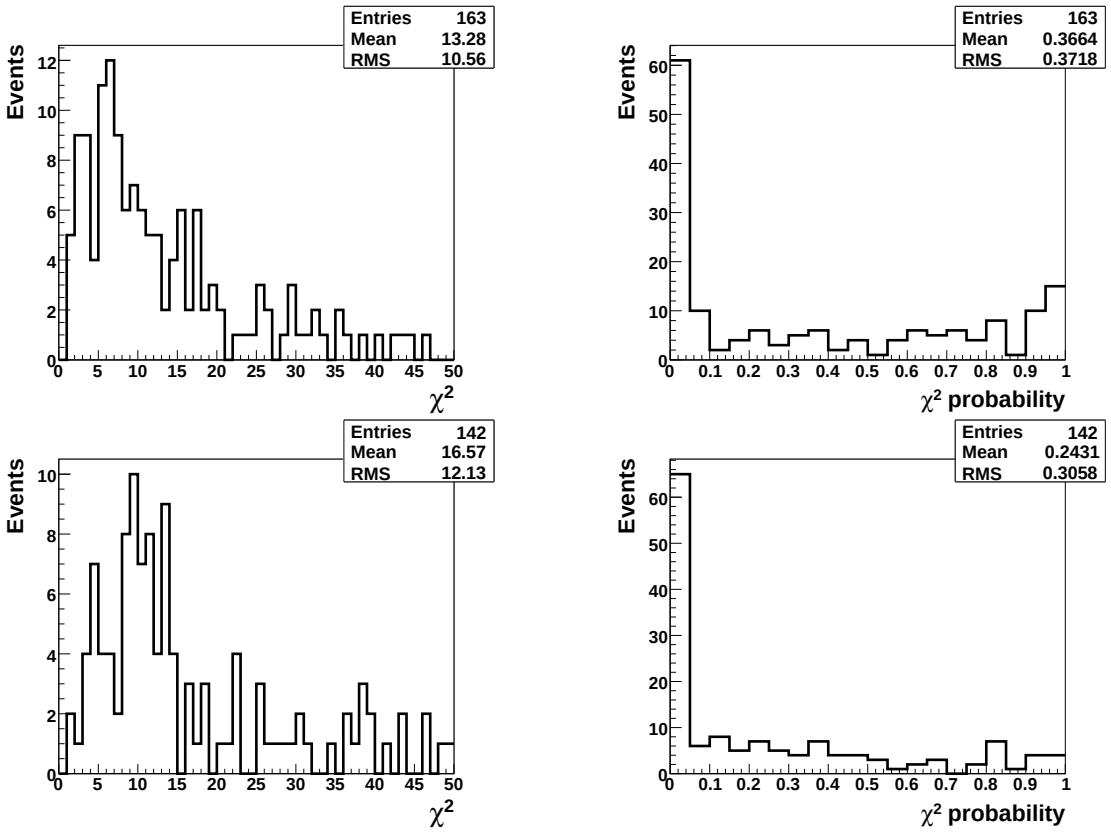

Figure 5.33: Upper plots: Susy background where one branch of the cascade meets the cascade that is searched for. Lower plots: The remaining Susy background. (200 events each)

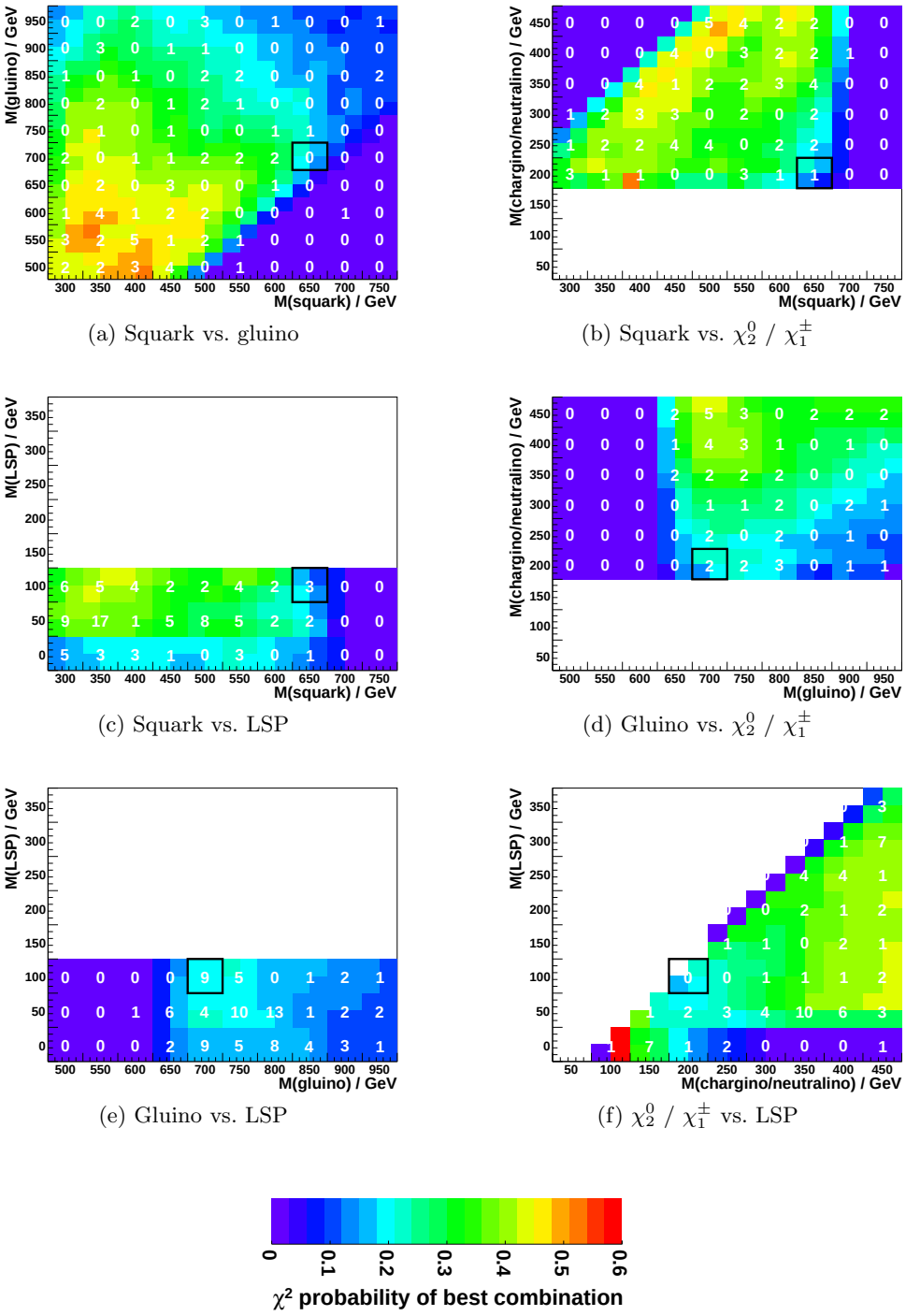

(a) Squark vs. gluino

(b) Squark vs. χ_2^0 / $\chi_1^\pm$

(c) Squark vs. LSP

(d) Gluino vs. χ_2^0 / $\chi_1^\pm$

(e) Gluino vs. LSP

(f) χ_2^0 / $\chi_1^\pm$ vs. LSP

Figure 5.34: Scans of two masses with the Susy background events only. The average of the χ^2 probability of the best combinatorial hypothesis per event in plotted.

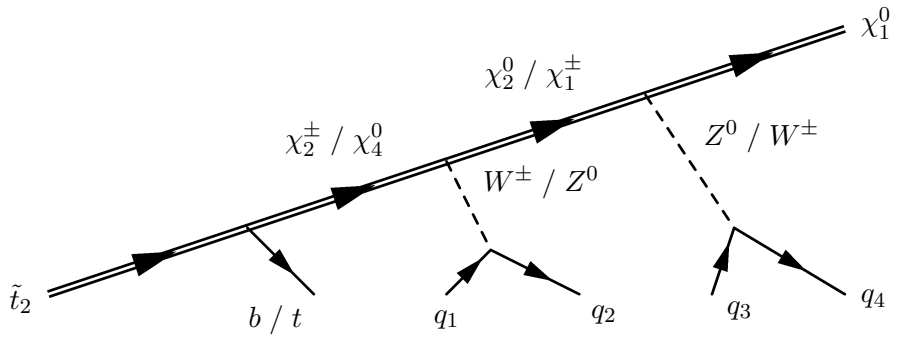

Figure 5.35: Dominant decay mode of the $\tilde{t}_2$ squark via two intermediate gauginos. Such decays might be misinterpreted as the gluino branch of the signal cascade.

In addition, events with the same cascade but with the much lighter top or bottom squarks are also in the background sample. Therefore the shift of the squark mass towards lower masses in the two upper and the middle left plots is comprehensible.

The $\chi_2^0/\chi_1^\pm$ is forced to larger masses (especially in the middle right and the lower right plot). For the signal selection of this analysis, only left-handed squarks are accepted since almost 100% of the right-handed squarks decay directly into the LSP without another gaugino as intermediate state. The topology of such a decay is the same as the decay of the $\chi_2^0/\chi_1^\pm$ in the signal events. Therefore it is to be expected that right-handed squarks are taken as $\chi_2^0/\chi_1^\pm$.

The LSP is unique and occurs in every Susy event twice at the end of each decay branch. In the plots where the LSP mass is scanned (middle left, lower right, and lower left) there is a high χ^2 probability in the region of the true mass, regarding the shifts caused by the other mass that is scanned.

The gluino has a special status in all events in this Susy scenario as well: It decays numerously over two supersymmetric intermediates into the LSP. In the middle right and the lower left plot the true gluino mass leads to better probabilities. However this uniqueness is often disturbed by final state radiation. That seems to be the case in the upper left plot.

Another reason why both the squark and the gluino masses tend to lower values in this plot can be found by considering the $\tilde{t}_2$ squark. A dominant decay channel is sketched in Fig. 5.35. There are two $Z^0/W^\pm$ bosons in this chain and, assuming them to decay hadronically, there are five jets from this branch. If one of the boson jets is rejected by the pre-selection cuts or maybe associated to the other branch, the gluino hypothesis would be forced to the $\tilde{t}_2$ mass (660 GeV) and the squark hypothesis to the $\chi_2^\pm/\chi_4^0$ mass (395 GeV). Since one of the jets has to be missing, the best hypothesis for the "gluino" mass should be even smaller than the $\tilde{t}_2$ mass.

Figure 5.34(b) shows a diagonal band of good hypotheses at lower squark and higher $\chi_1^\pm/\chi_2^0$ masses. A possible explanation is the occurrence of the $\tilde{t}_1$ squark in the decay

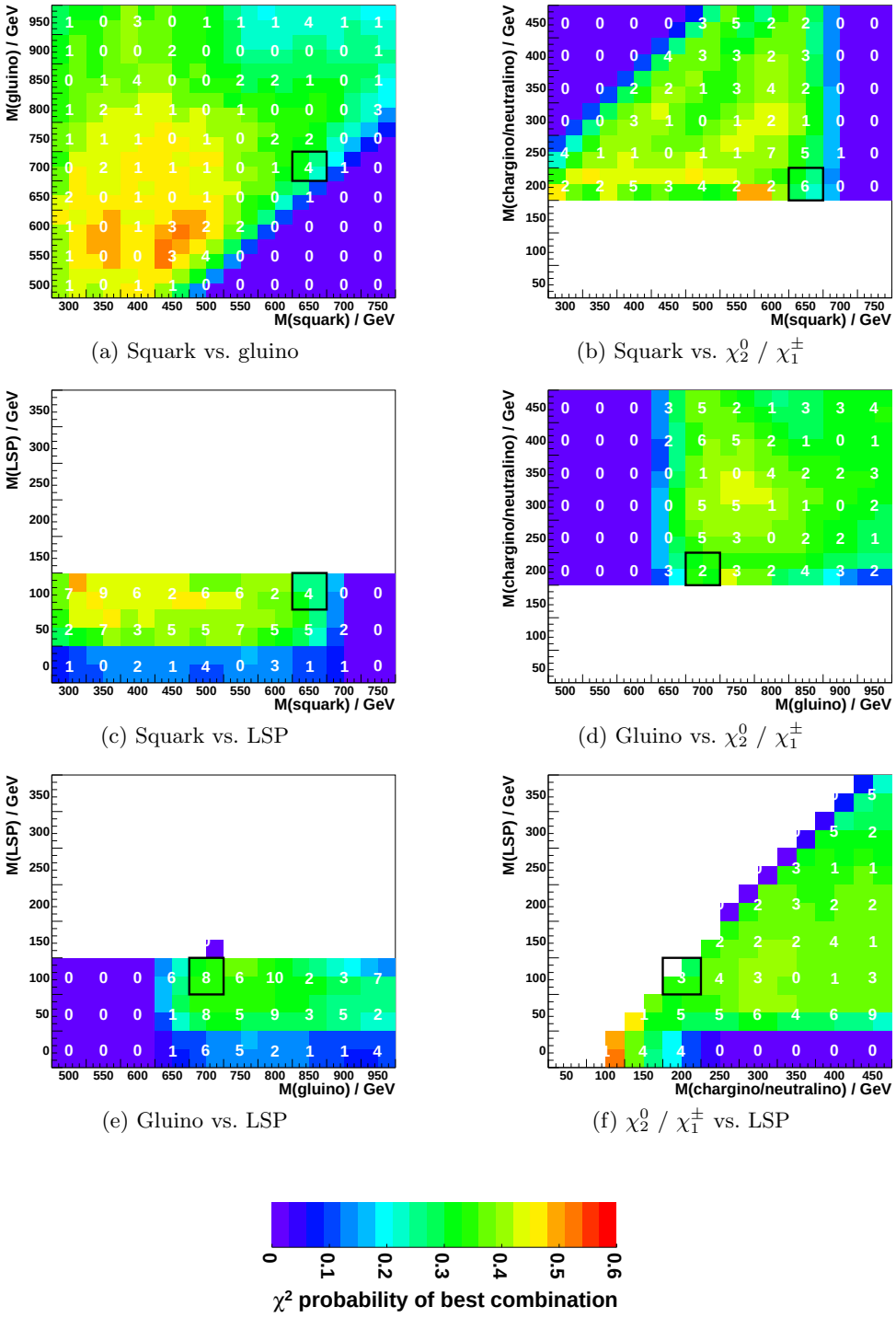

(a) Squark vs. gluino

(b) Squark vs. χ_2^0 / $\chi_1^\pm$

(c) Squark vs. LSP

(d) Gluino vs. χ_2^0 / $\chi_1^\pm$

(e) Gluino vs. LSP

(f) χ_2^0 / $\chi_1^\pm$ vs. LSP

Figure 5.36: Scans of two masses with the Susy background sample with one decay branch that agrees with the signal decay.

chain. The $\tilde{t}_1$ squark with a mass of about 500 GeV is the lightest squark within this Susy scenario. The branching ratio of a decay into a $\chi_2^{\pm}$ (395 GeV) is much higher than those of the other squarks. The $\tilde{t}_1$ prefers a hypothesis with a lower squark mass and the $\chi_2^{\pm}$ prefers a hypothesis with a higher $\chi_1^{\pm}/\chi_2^0$.

In Fig. 5.36 the two-dimensional scans are plotted for the events which have one decay branch from the signal cascade. The results are very similar to the cascades which don't fit to the signal cascade at all (Fig. 5.34).

5.3.7 Signal and Susy Background

Finally signal and background will be combined. The last information that is taken from Monte Carlo has been the assignment weather an event has the signal cascade or not. The χ^2 probabilities shown in the previous plots of signal, background, and background with one signal branch are weighted with their abundance in the data sample and combined to one plot mass scan. The results of the two-dimensional scans are plotted in Fig. 5.37. The scanning ranges are spread in some of the plots to show a larger area where the background events have good probabilities.

The method of presentation in this thesis is not able to separate the signal from the background. The maxima in the regions of the true masses vanish which have been seen in the plots with only the signal events. Although the probabilities of the signal are better than those of the background, they are lost by averaging with the huge amount of background events.

The gluino and the LSP masses have maxima in the regions of the true masses, but these have been seen in the plots where the background has been analyzed separately as well.

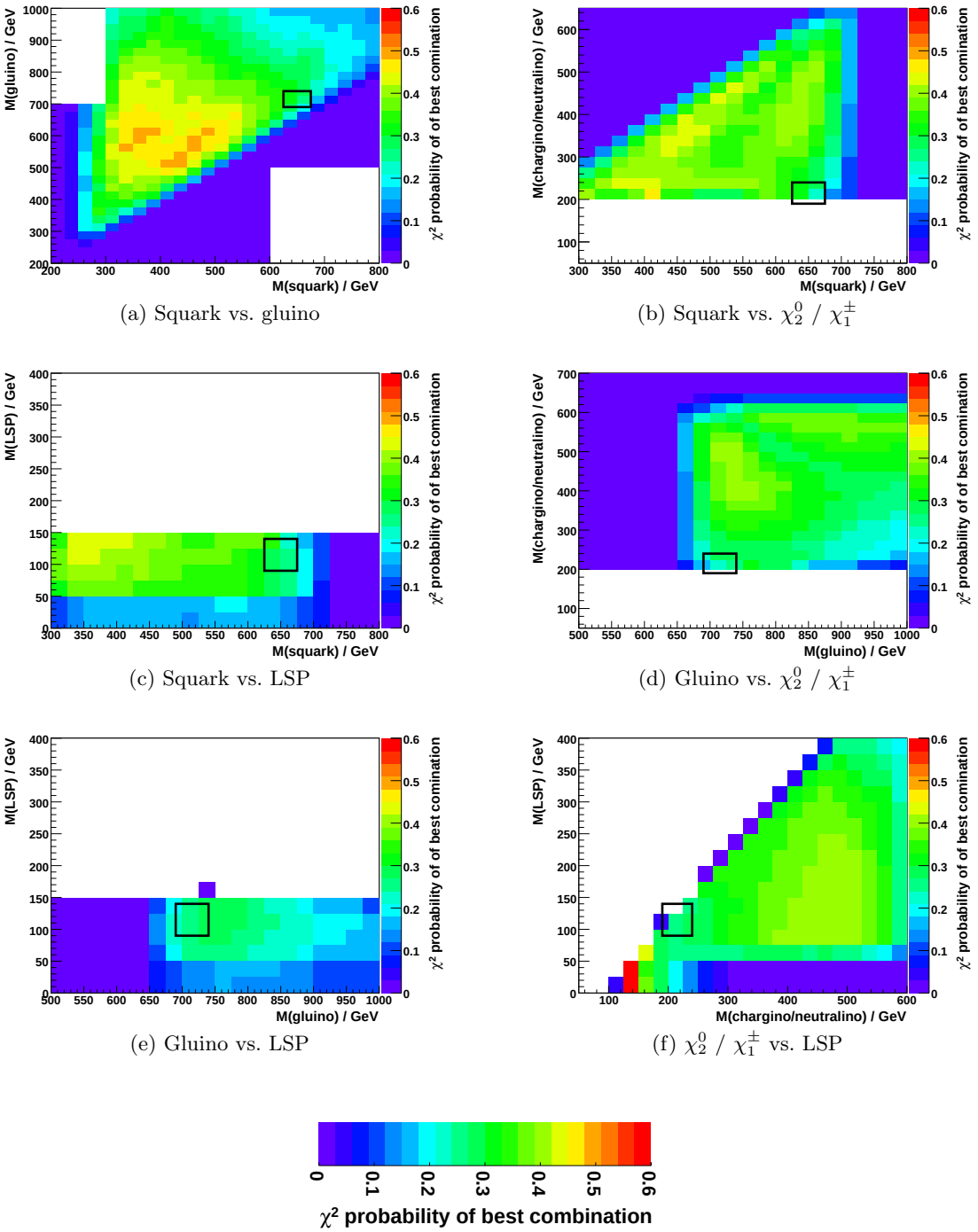

(a) Squark vs. gluino

(b) Squark vs. χ_2^0 / $\chi_1^\pm$

(c) Squark vs. LSP

(d) Gluino vs. χ_2^0 / $\chi_1^\pm$

(e) Gluino vs. LSP

(f) χ_2^0 / $\chi_1^\pm$ vs. LSP

Figure 5.37: Scans of two masses with the signal and Susy background: The background with one decay branch from the signal and the other Susy background is combined with the signal according to their abundance.

6 Summary

In this study the method of kinematic fitting has been applied to determine the mass parameters of intermediate states occurring in long decay chains. A Monte Carlo simulated mSUGRA signal sample has been analyzed within two scenarios: One is called "truth" scenario the other "realistic" scenario.

Within the "truth" scenario Monte Carlo information has been used to select the jets and to associate them to the partons from the Susy particle decays. The mass hypothesis for the Susy particles has been varied to find the hypothesis with the highest probability. In the region of the true masses significantly better χ^2 probabilities have been found for each Susy particle. The scanning has been done in three steps: First each mass has been scanned separately while the other masses have been fixed at the true values. Second, all combinations of two masses have been scanned simultaneously to find correlations between them. The last step has been the simultaneous scan of all four Susy masses that are involved in the signal cascade. In all these scans good agreements with the true masses have been found.

Within the "truth" scenario it has been shown that the method works. If the combinatorial background can be suppressed and the jets can be selected properly, the kinematic fit is a good technique to determine the mass parameters of supersymmetric particles.

Within the "realistic" scenario the analysis has been redone in a way that corresponds to the real data case. The full combinatorial background has been taken into account. The ranges of good hypotheses for the Susy masses are consequently wider. But still, large parts of the parameter space can be excluded.

Within the "realistic" scenario the background from other Susy events has been subjected to the fitting procedure. It has been shown that the probabilities for these events are worse.

Outlook

The logical next step would be to consider the background of Standard Model events. The largest backgrounds are expected from QCD events with lots of jets and fake missing transverse energy and from $Z^0 \rightarrow \nu\bar{\nu} +$ jets events. Nevertheless, the overall Standard Model background contribution is expected to be small [16]

The combinatorial problem can be reduced by analyzing a cascade with leptons in the final state. The same cascade can be used but with at least one $Z^0/W^{\pm}$ decaying into e^+ e^- or μ^+ μ^-, for example.

The usage of data can be extended into two directions: First, the relations between the masses predicted by mSUGRA at the electroweak scale can be used. This can be done by scanning over the mSUGRA parameters instead of the masses themselves. In addition, other variables which distinguish between various mSUGRA parameters as the cross section can be combined with the result of the fit. Secondly, the technique should be studied within other New Physics scenarios. The first step would be other mSUGRA benchmark points, but in principle all models which predict decays with several massive intermediate states and not too much unmeasurable particles in the final state can be handled with kinematic fits.

The procedure that has been presented can be further improved. The analysis of the Susy background events has shown that other event topologies lead to good probabilities in other mass regions. This should be studied in detail to understand which event topologies can be included as another signal definition. The method can be extended to cover simultaneously many different event topologies. The determination of the mass of one Susy particle in different event topologies might allow to give more accurate limits on this mass.

Another problem is the finding of suitable initial values and the parametrization of the unmeasured LSPs. A parametrization using the whole kinematic information about the LSP momentum could be worth.

The averaged χ^2 probability that has been used in this thesis is a good measure for a qualitative analysis. A thorough statistical interpretation of the resulting χ^2 needs to be evaluated.

The combination of the signal with the background has shown that the signal cannot be separated by the used method only, but nevertheless it might provide a useful information, that e. g. could be used as input in a multivariate analysis.

Bibliography

[1] David Griffiths. *Intruduction to Elementary Particles*. Wiley-VCH, 2 edition, 2008.

[2] http://pi.physik.uni-bonn.de/%7Ebrock/feynman/vtp_ws0506/. [Online; accessed 7-April-2009].

[3] Vernon Barger and Roger Phillips. *Collider Physics*. Frontiers in Physics. Addison-Wesley, 1987.

[4] G. Abbiendi et al. Search for the standard model Higgs boson at LEP. *Physics Letters B*, 565:61, 2003.

[5] The TEVNPH Working Group. Combined CDF and DØ upper limits on the Standard Model Higgs-boson production with up to $4.2\,\mathrm{fb}^{-1}$ of data. *arXiv:hep-ex*, 0903.4001v1, 2009.

[6] S. Abdullin et al. Summary of the CMS potential for Higgs boson discovery. *Eur Phys J C*, 39, 2005.

[7] Stephen Martin. A supersymmetry primer. *hep-ph/9709356*, 1999.

[8] Douglas Clowe et al. A direct empirical proof of the existence of dark matter. *Astrophysical Journal Letters*, 648:109, 2006.

[9] S. Fukuda et al. Solar ^{8}B and hep neutrino measurements from 1258 days of Super-Kamiokande data. *Physical Review Letters*, 86:5651, 2001.

[10] Q. Ahmad et al. Direct evidence for neutrino flavor transformation from neutral-current interactions in the sudbury neutrino observatory. *Physical Review Letters*, 89:011301, 2002.

[11] Sidney Coleman and Jeffrey Mandula. All possible symmetries of the S matrix. *Physical Review*, 157:1251, 1967.

[12] Rudolf Haag, Jan Łopuszański, and Martin Shonius. All possible generators of supersymmetries of the S matrix. *Nuclear Physics*, B88:257, 1975.

[13] Aran Garcia-Bellido. Searches for gauge mediated supersymmetry breaking at ALEPH with centre-of-mass energies up to 209 GeV. *CERN-Thesis*, 41, 2002.

[14] Nobelprize.org. http://nobelprize.org/nobel_prizes/physics/laureates/2004/public.html. [Online; accessed 26-March-2009].

[15] H. Nishino et al. Search for proton decay via $p \to e^+\pi^0$ and $p \to \mu^+\pi^0$ in a large water Cherenkov detector. *arXiv*, 0903.0676, 2009.

[16] The CMS Collaboration. CMS physics technical design report, volume II: Physics performance. *J. Phys. G*, 34, 2007.

[17] CERN document server. http://cdsweb.cern.ch/. [Online; accessed 27-February-2009].

[18] The CMS Collaboration. The CMS experiment at the CERN LHC. *JINST*, 3, 2008.

[19] Volker Blobel and Erich Lohrmann. *Statistische und numerische Methoden der Datenanalyse*. Teubner Studienbucher, 1998.

[20] Jorge Nocedal and Stephen J. Wright. *Numerical Optimization*. Springer Series in Operations Research. Springer, 2 edition, 2006.

[21] Mark Thomson, on behalf of the Electroweak Working Group. Measurement of the mass of the W boson at LEP. *Eur Phys J C*, 33, 2004.

[22] The BaBar Collaboration. Measurments of moments of the mass distribution in semileptonic B decays. *Phys Rev D*, 69, 2004.

[23] J. D'Hondt et al. Fitting of event topologies with external kinematic constraints in CMS. *CMS Analysis Note*, 25, 2005.

[24] http://aleph.web.cern.ch/aleph/ hansenjo/ALEPH-ONLY/abcfit/abcfit.html. [Online; accessed 2-April-2009].

Danksagung

Ich bedanke mich bei Prof. Dr. Peter Schleper dafür, dass er mir ermöglich hat, in diesem spannenden Themenfeld meine Diplomarbeit zu machen, für die Betreuung und die motivierenden und hilfreichen Hinweise.

Bei Dr. Christian Sander und Dr. Christian Autermann möchte ich mich für die intensive Betreuung und die vielen Ratschläge und Hilfestellungen bedanken. Benedikt Mura danke ich für die Hilfe beim Korrekturlesen.

Für die angenehme Arbeitsatmosphäre, die schnellen Antworten bei kleineren Problemen danke ich allen Postdocs, Doktoranden und Diplomanden der Arbeitsgruppe.

Erklärung

Hiermit erkläre ich, dass diese Diplomarbeit von mir persönlich und nur unter Verwendung der angegebenen Quellen erstellt wurde. Sie wurde so oder in ähnlicher Form bisher keiner Prüfungskommission vorgelegt. Mit der Veröffentlichung bin ich einverstanden.

Hannes Schettler
Hamburg, den 9. April 2009